

Chapter 2

Introduction to NMR Studies of Metals, Metallic Compounds, and Superconductors

NMR studies of high- T_c materials and other correlated-electron systems developed in a context of many years of NMR studies of conventional superconductors as well as of d-band transition metals, alloys, and intermetallic compounds. It is therefore appropriate to begin this volume with a brief review not only of the NMR probe, itself, but of the general physical phenomena probed by NMR in metals, alloys and intermetallic compounds, in both the normal and superconducting states. The published literature on this subject matter is, of course, vast, and the references cited here will necessarily be rather limited. We begin by citing the standard works on nuclear magnetism by Abragam [5] and Slichter [6], where many basic NMR phenomena are derived and discussed. These sources also present an extensive guide to the early literature, which the interested reader will find highly informative. For NMR of metallic systems, there are thorough reviews by Narath [7] and Winter [8] and for early NMR studies on superconductivity, there is a detailed and informative review by MacLaughlin [9]. We shall also have recourse to the treatments of superconductivity by Tinkham [18] and Schrieffer [19]. Relevant reviews of high- T_c NMR studies will be cited at the beginning of Chap. 3.

2.1 The Fundamental Elements of NMR

The foundation of nuclear magnetic resonance (NMR) rests on the fact that many stable isotopes in the periodic table possess a nonzero spin quantum number I and, thus, angular momentum $\hbar I$ and a magnetic moment $\mu = \gamma \hbar I$, where γ is the nuclear

gyromagnetic ratio. In an applied magnetic field \mathbf{H} , a nuclear moment $\boldsymbol{\mu}$ has an energy $-\boldsymbol{\mu} \cdot \mathbf{H}$ and in classical terms undergoes a torque $\boldsymbol{\tau} = \boldsymbol{\mu} \times \mathbf{H}$.¹ Equating this torque to $\hbar d\mathbf{I}/dt$, one finds an equation leading to Larmor Precession of the component of $\boldsymbol{\mu}$ transverse to the field \mathbf{H} . The latter may be written $\boldsymbol{\mu} - \hat{\mathbf{u}}(\boldsymbol{\mu} \cdot \hat{\mathbf{u}})$, where $\hat{\mathbf{u}} = \mathbf{H}/|\mathbf{H}|$ is a unit vector parallel to \mathbf{H} . In this way, the Larmor Precession Frequency emerges as $\omega_0 = \gamma H$. This is the basic nuclear magnetic resonance (NMR) frequency. In the contrasting case of nuclear quadrupole resonance (NQR), there is no Larmor precession effect, because the nuclear energy splitting is provided by quadrupolar coupling with a local electric field gradient (EFG). This effect may, however, still be called a “magnetic resonance”, because the resonance is excited with an rf field that couples with the magnetic moment $\boldsymbol{\mu}$, and the signal is received by magnetic induction.

If we add to the foregoing torque equation of motion the terms $-\hat{\mathbf{u}}(\boldsymbol{\mu} \cdot \hat{\mathbf{u}} - \mu_0)/T_1$ and $-\boldsymbol{\mu} + \hat{\mathbf{u}}(\boldsymbol{\mu} \cdot \hat{\mathbf{u}})/T_2$ to embody the longitudinal (T_1) and transverse (T_2) relaxation processes, one arrives at the celebrated Bloch equation model for NMR spectroscopy [10]. Here, $\mu_0 = \gamma^2 \hbar^2 I(I+1)H/3k_B T$ is the thermal equilibrium nuclear moment in a field H . The Bloch equations lead to nuclear resonance spectra of Lorentzian form with a width parameter $\langle \Delta\omega \rangle = (1/T_1 + 1/T_2)$ and are well suited to the study of NMR lines in liquids [11]. For NMR of nuclei embedded in condensed matter, however, there arise many complexities that go beyond the Bloch equations. A basic discussion of these effects is given below in this section of Chap. 2.

The essence of pulsed NMR is to excite nuclear induction signals through the application of radiofrequency (rf) pulses of oscillating magnetic field $2H_1 \cos(\omega t)$ along an axis perpendicular to \mathbf{H} . We illustrate here very briefly the action of such pulses [10] with the simple case of a narrow NMR line excited at its precise NMR frequency $\omega = \omega_0(1 + K)$, where K is the NMR shift, here taken to be isotropic for simplicity. The action of the pulse must take place in a time t_w short compared with $T_{1,2}$, after which the nuclear magnetization will take the value $M_0[\hat{\mathbf{u}} \cos(\gamma H_1 t_w) + (\hat{\mathbf{u}} \times \mathbf{H}_1) \sin(\gamma H_1 t_w)/H_1]$ in a reference frame rotating in synchrony with the rotating field H_1 . The pulse width t_w may be adjusted so that $\gamma H_1 t_w = \pi/2$ to obtain the maximum transverse component followed by a free-induction signal, or it may be adjusted so that $\gamma H_1 t_w = \pi$, after which there is no transverse component, but a maximum inverted magnetization $-\hat{\mathbf{u}}M_0$, as the first step in a T_1 measurement. The first of these is known as a “ $\pi/2$ -pulse”, and the second is known as a “ π -pulse” or an inversion pulse. In practice, circumstances frequently don’t permit such precise conditions to be achieved, because of linewidths comparable to or greater than the value of H_1 used, or non-uniform values of H_1 over the sample. In spite of small problems such as these, the practitioner frequently speaks of “ $\pi/2$ -pulses” and “ π -pulses” as an idealization of what actually occurs. The action of (rf) pulses under more general circumstances is discussed in Appendix A, where spin echoes are also described in some detail.

¹Correctly, the field in the magnetic torque expression is the magnetic induction. We use the symbol \mathbf{H} in keeping with the traditional literature.

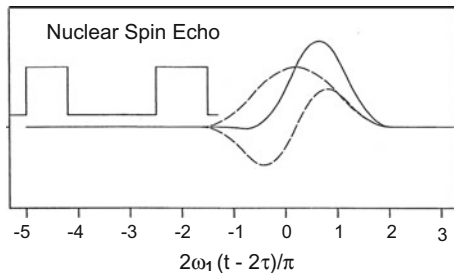


Fig. 2.1 A simulated spin echo signal is shown (solid curve), corresponding to the $(0.8\pi/2, \pi/2)$ pulse pair (shown) applied to a broad, inhomogeneous distribution of NMR frequencies. The echo is the sum of two contributions which are symmetric and antisymmetric, respectively, (dashed lines) with respect to the center point of the echo. The latter point is at time $2\tau + t_{w2} - t_{w1}$ from the leading edge of the first pulse, where τ is the time interval between the leading edges of the pulses and t_{w1}, t_{w2} are the respective pulse widths [24]

The basic effects one typically measures and interprets in NMR studies of solids consist of the shape and structure of the spectrum, the frequency shift tensor $\mathbf{K}_{\alpha\beta}$, and the longitudinal (T_1) and transverse (T_2) relaxation processes. The acquisition and interpretation of these basic data will be the preoccupation of most of this volume, since each of these elements can provide important information about the solid state environment surrounding nuclear sites. Here we wish simply to introduce them, and in this section (2.1) the basic definition, measurement and interpretation of these parameters will be reviewed. A detailed description of spin echo excitation and behavior are given in Appendix A.

2.1.1 Observation of NMR/NQR Signals

In the early days of solid-state NMR, it was customary to employ continuous wave (CW) methods to observe NMR signals. Techniques such as the marginal oscillator and the popular crossed-coil *rf* bridge spectrometer manufactured by Varian Associates, as well as home-built *rf* bridges, were used to obtain a wealth of useful NMR data. Compared with pulsed NMR this method has, however, a number of inherent drawbacks, such as (i) it is not useful for severely broadened lines, (ii) it cannot distinguish between static and dynamic line broadening, so that (iii) it cannot measure the dynamic transverse relaxation time T_2 , nor short values of T_1 , to name just a few. Thus, it gradually gave way to pulse methods for solid-state NMR studies [22]. While we do not discuss CW NMR methods in any detail here, it must be noted that important NMR data on solids have been reported that were taken using CW techniques. A prominent example is a study of the Kondo effect by Boyce and Slichter [323, 324] discussed in Chap. 8.

Free Induction and the Spin Echo

Following a single *rf* pulse as described above in the introduction, one can often observe a *free-induction decay* signal with the form

$$F(t) = F_0 \cos[(\omega_c - \omega_{rf})t] \int_{-\infty}^{+\infty} G(\omega_c + \omega) \cos(\omega t) d\omega, \quad (2.1.1)$$

where $G(\omega_c + \omega)$ is a symmetric lineshape function centered on ω_c , and ω_{rf} is the frequency of the *rf* pulse and of the phase detector used to display the signal. In (2.1.1), the *rf* excitation pulse field is assumed to be large compared with the linewidth, so the pulse angle is uniform across the spectral width. In this simplified case, it is seen that $F(t)$ is simply the cosine transformation of the lineshape $G(\omega)$ and vice versa. The difficulty of determining $G(\omega)$ this way is that the early part of $F(t)$ is masked by the dead time of the receiver. Not infrequently, the decay time T_2^* is so short that very little of $F(t)$ can actually be recorded. For these reasons, the preferred method for extracting $G(\omega)$ with pulsed NMR is via the *spin echo*.

Nowadays, the *spin echo* [23] is used almost universally for measurements and observation of NMR/NQR signals in solids. Here we describe the basic features of the spin echo and illustrate its use in a simple case. A much more detailed discussion of echo formation and of the echo decay processes addressed below is given in Appendix A. Following an initial ($t = 0$) pulse such as that described above, a second pulse called the refocusing pulse is applied at the same frequency at $t = \tau$. For simplicity, we also assume the latter pulse has the same phase as the first pulse.² We also assume uniform excitation across the whole spectrum as in (2.1.1).

Taking the leading edge of the first pulse as time zero, then the second pulse at time τ is followed by a spin-echo signal at time 2τ . The mechanism of this effect is very simple. The second pulse effectively inverts the dephasing that has occurred during time τ , so that after the second pulse, the phase deviations of the precessing nuclei unwind and return to zero at time $2\tau + t_{w2} - t_{w1}$. In this way the macroscopic transverse magnetization that generates an observable NMR signal is restored.

We give here the expression for a spin echo for the same simple case of a uniformly excited, symmetric lineshape function $G(\omega)$ that was assumed for the free-induction signal in Ex. (2.1.1). Thus, we again assume that the *rf* field H_1 is much greater than the width of $G(\omega)$, i.e. $\langle \Delta\omega \rangle / \gamma$ (in field units). In that limit, the precessing nuclear magnetization that makes up the principal component of the echo signal is given by

$$E(t) = -\frac{1}{2} \sin(\omega_1 t_{w1}) [1 - \cos(\omega_1 t_{w2})] \cos[(\omega_c - \omega_{rf})(t - t_E)] \int G(\omega_c + \omega) \cos[\omega(t - t_E)] d\omega, \quad (2.1.2)$$

where t_{w1} and t_{w2} are the widths of the two *rf* pulses, respectively, and $t_E = 2\tau + t_{w1} - t_{w2}$ is the center point of the spin echo, measured from the beginning of the first pulse. The maximum amplitude of the echo is obtained with $\omega_1 t_{w1} = \pi/2$ and

²Phase manipulation on the refocusing pulse to achieve special effects with spin echo studies is discussed in detail in Appendix A.

$\omega_1 t_{w2} = \pi$, giving the same expression as for the FID in (2.1.1), except with its sign inverted. Furthermore, (2.1.2) allows both positive and negative values of $t - t_E$, so that the shape of the echo signal in time is very much like two free-induction signals back to back. In this way, one is able to move the signal away from the excitation pulses so that it can be measured and recorded without interference from pulse transients.

We note two additional requirements for the observability of spin echoes in any given case. The echo signal represented by (2.1.2) will always decay as time τ increases. This decay time is denoted T_2 in the literature and is known as the *dynamic decay time*. See the next subsection for a discussion of this parameter. Thus, (2.1.2) only holds as written for $T_2 \gg 2\tau$.

A second requirement for observability of spin echoes is that the nuclear spins concerned must have a source of *static broadening* that is greater than any relevant dynamic decay process. A detailed discussion of such matters is given in the next subsection. Thus, the NMR line under study must have a “static width” greater than its “dynamic width” for spin echoes to be feasible. If the *rf* field H_1 is greater than the static width of the line, then the *rf* pulse will excite an echo signal from all of the nuclei. Otherwise, it will excite just a subset of nuclei centered on the carrier frequency of the pulse. In many cases the static width of the spectrum is much greater than H_1 . A remarkable property of the spin echo is that it can be employed to very accurately record the detailed shape of such a static spectrum. The basis for such a capability is discussed next.

We touch here briefly on an important point regarding the frequency resolution of spin-echo spectroscopy, which is discussed in detail in Appendix A. Since the NMR signals are excited using pulse fields H_1 of typically 100 Gauss amplitude, one might suppose that these large fields would limit the available frequency resolution to $\sim \gamma H_1$. However, this is not the case. It is straightforward to demonstrate that the total area under the spin echo waveform is proportional to the line intensity at the frequency of excitation to within a very narrow bandwidth. The resolution obtained in this way is formally independent of the magnitude of the excitation field H_1 , but is actually determined by the time frame over which the echo can be integrated. See Appendix A for more details. An example of a (simulated) spin echo generated somewhere in the center of a broad, inhomogeneous NMR line is displayed in Fig. 2.1. On the other hand, in the opposite limit that H_1 is actually much greater than the static linewidth, an excellent way to record the NMR spectrum is simply to Fourier transform the echo waveform as suggested by (2.1.2).

The question of observability of spin-echo signals is an important one for the NMR spectroscopist. We note here that solid-state NMR signals are typically of the order of microvolts, with expected raw signal-to-noise ratios which are typically of the order of unity or less. Thus, one cannot overemphasize the importance of digital signal averaging methods to the success of modern pulsed NMR technique. The great majority of solid-state NMR studies reported nowadays have used digital signal averaging to improve the signal-to-noise ratio. It is also possible to estimate the available NMR signal strength given reasonable estimates of the experimental parameters.

2.1.2 Definition and Interpretation of NMR Parameters: T_2 Processes

T_2 processes are the decay of NMR signals in time, *i.e.*, of coherent, transverse nuclear magnetization. There are two T_2 parameters in common use, namely the spin echo decay time constant T_2 and that of the free induction decay T_2^* . T_2 decay is strictly a dynamic effect, while T_2^* combines static and dynamic components. When, as is often the case, one has $T_2 \gg T_2^*$, then T_2^* will be dominated by purely static broadening processes. It is important to note that for (2.1.2) to represent an actual spin echo, one has to have $T_2 \gg T_2^*$ for that to be possible. And while there are many very simple compounds where that condition is not fulfilled, it is rare for solid state systems with interesting and even exotic properties to have the foregoing condition fail.

Let us examine the types of hyperfine interactions that contribute to T_2 and T_2^* decay effects. We note at the outset that a useful formal treatment of spin echo decay has been given by Alloul and Froidevaux [294]. Here, we give a brief discussion of dynamic processes that contribute to T_2 decay. There are several general classes of hyperfine fluctuation that can be distinguished, namely spin-spin interactions, spin-lattice interactions, and spin-flip interactions that are imposed by applied *rf* fields. Finally, since spin echoes are relaxed by any change in the local magnetic environment at the relevant nuclear spin sites, one must include physical diffusion of ions that carry the nuclear spins. We shall not, however, discuss this mechanism except simply to mention it.

Let us first consider nuclear spin-spin couplings. These consist mainly of the dipolar,³ pseudo-dipolar, [28] and RKKY [27] exchange interactions. There are several points about these interactions that need to be addressed in the context of spin-echo decay. First, which interactions are ‘allowed’ in such a discussion? We take the *z* axis as the ‘quantization axis’ in the problem, *i.e.* the Zeeman term $\mathcal{H}_Z = -\hbar\omega_0 \sum_i I_{zi}$ is the principal nuclear spin energy term. Then, spin-spin coupling terms are only ‘secular’ (*i.e.*, effective) if they commute with \mathcal{H}_Z . Thus, terms of the following form are generally admissible.

$$\mathcal{H}_{ss} = \sum_{i,j} A_{ij} I_{zi} I_{zj} + \sum_{i,j} B_{ij} (I_{+i} I_{-j} + I_{-i} I_{+j}) + \sum_{i,j} D_{ij} I_{zi} I'_{zj} + \cdots, \quad (2.1.3)$$

where the prime indicates a different, non-resonant nuclear species in the same crystal structure, and the dots indicate that other terms involving non-resonant (“unlike”) spins are omitted. However, what effect would, *e.g.*, the D_{ij} terms have on the decay process of (a) coherently precessing nuclear magnetization represented by $I_x = \sum_i I_{xi}$ or (b), on a spin echo generated via the unprimed, resonant nuclei? The answers for these two cases can be markedly different.

³Dipolar couplings are discussed in detail by Abragam [5], Chap. IV, and by Slichter [6], Chap. 3.

With typical dipolar couplings the FID and spin-echo decays are similar, but not identical. What can make a great deal of difference is inhomogeneous broadening that is non-uniform on a local level. The Hamiltonian term would have the form $-\sum_i \Delta\omega_i I_{zi}$, where $\Delta\omega_i$ is a static quantity that varies by an amount equal to or greater than dynamic, interactive broadening terms at the local level. Such terms will contribute substantially to T_2^* decay, but will tend to inhibit spin-echo decay, making T_2 longer. Terms like this arise from local crystalline disorder, imposing modulation on the NMR shift mechanism. They prevent terms such as the B_{ij} terms in (2.1.3) from driving local spin fluctuation processes, because variations in the local resonant frequencies (i.e., the $\Delta\omega_i$ terms) prevent flip-flop fluctuations from conserving energy. The resulting static interaction environment does not contribute to the spin-echo decay process.

A second type of local coupling that can relax the FID, but may not affect the spin-echo is the “zz” unlike spin term D_{ij} of the previous paragraph. If the primed spin system has local fluctuations driven by $I'_{\pm i} I'_{\mp j}$ fluctuations, then the D_{ij} terms shown there will contribute to both the T_2 and T_2^* relaxation processes. However, it is not unusual for such unlike spins to be essentially static, whereupon they will make no contribution to the T_2 (spin-echo) decay. Of course, long-range inhomogeneity also contributes to T_2^* decay, but not to T_2 . When such broadening becomes greater than γH_1 , then $1/T_2^* \sim \gamma H_1$.

A second contributor to spin-echo decay is reversal of neighboring nuclear-spin orientations by the refocusing pulse. This mechanism makes use of the A_{ij} terms in \mathcal{H}_{ss} . If such a set of $I_{zi} I_{zj}$ terms are rendered static by their environment, such as happens in certain high- T_c systems,⁴ the only way such terms can be made to contribute to T_2 decay is via the refocusing pulse. The magnitude of this effect depends on the pulse angle used for the measurement, with maximum effect taking place for a π pulse. This variation of the $I_{zi} I_{zj}$ broadening can also be used to separate this effect from other T_2 processes that do not vary with pulse angle.

Another interesting possibility is to employ terms of the D_{ij} form in a *spin-echo double resonance* scheme by applying *rf* pulses at the NMR frequency of an unlike, i.e., primed spin species while monitoring the echo signal from the unprimed spins. In the event that an appreciable fraction of the primed spins are reversed by the second pulse, a measurable degradation of the unprimed-spin signal will be recorded. By scanning the frequency of the primed-spin pulse, one can map out the primed-spin NMR line without ever observing that NMR signal directly. This has been used in studies of nuclear species that are difficult to observe directly [270]. This technique is known as spin-echo double resonance (SEDOR).

A third mechanism of T_2 decay occurs through T_1 processes. Only in a rather small subset of cases is T_1 a significant factor in the T_2 process, simply because in many instances $T_1 \gg T_2$. As suggested by the Bloch equations mentioned above, $1/T_1$ is a contribution to the linewidth in general, but the situation is a bit more nuanced than that. The T_1 process contributes, of course, to both $1/T_2$ and $1/T_2^*$. This is not a particularly useful effect, but mostly just something one has to watch out for. There is one small corner of parameter space where the T_1 effect on spin-echo decay is

⁴See the discussion of the Pennington-Slichter indirect coupling and its measurement in Chap. 6.

a bit more interesting and useful. This is in the case of odd half-integral nuclear-spin quantum numbers I , where all but the central $\pm 1/2 \leftrightarrow \mp 1/2$ transition are heavily broadened by electric-field gradient noise (i.e., “quadrupolar broadened”), so that only the central transition is resolved. This circumstance arises in a surprising number of cases in practice. The upshot of it is that one finds a contribution to the echo decay that is enhanced by a factor $(I + 1/2)^2$ [284]. Thus,

$$1/T_2 = (1/T_2)_{\text{spin-spin}} + (I + 1/2)^2/T_1, \quad (2.1.4)$$

where the first term is the sum total of the other decay processes discussed above. In metallic host materials the T_1 term can often be identified, because it is Korringa-like, i.e. $1/T_1 \propto T$, while the spin-spin term is typically independent of T . There are corresponding enhancements for other $m \leftrightarrow m + 1$ transitions if their spin-echo signals can be observed in isolation, but it is only when all transitions of a given nuclear spin can be excited at once that the echo decay enhancement is simply $1/T_1$. The latter holds whenever $I = 1/2$.

Phenomena related to observation and relaxation of spin echoes are also discussed in more formal detail in Appendix A [294].

2.1.3 The Basic Structure of NMR Spectra in Solids

While many NMR phenomena can be understood in classical terms (e.g. the Bloch equations), nuclear spins are fundamentally quantum in nature, and their physics must be discussed in quantum mechanical terms to obtain a complete picture. As such, they can interact with their microscopic surroundings in highly complex ways, which is what allows the study of NMR properties to provide important microscopic information on the physical properties of host solids. Nuclei with spin quantum numbers $I > \frac{1}{2}$ also possess electric quadrupole moments, denoted Q , which then couple to static and fluctuating electric field gradients (EFG) generated by electric charge distributions in their environment. This adds to the richness and complexity of NMR spectra.

The basic nuclear spin Hamiltonian for spectra is given by (2.1.5), including both the Zeeman term representing the effect of an applied field \mathbf{H} and a quadrupolar term representing the interaction of the nuclear quadrupole moment with the electrical field gradient (EFG) tensor $V_{uv} = \frac{\partial^2 V}{\partial u \partial v}$ at the nuclear site in question (see [5], Chap. VI). Thus,

$$\mathcal{H}_{\text{spec}} = -\gamma \hbar \mathbf{I} \cdot (\hat{\mathbf{1}} + \hat{\mathbf{K}}) \cdot \mathbf{H} + \frac{e^2 q Q}{4I(2I - 1)} [3I_z^2 - I(I + 1) + \frac{\eta}{2}(I_+^2 + I_-^2)], \quad (2.1.5)$$

where $\hat{\mathbf{K}}$ is the NMR shift tensor and $\hat{\mathbf{1}}$ is the unit tensor. In this equation we use conventional notation, where $q = |\frac{\partial^2 V}{\partial Z^2}| = V_{ZZ}$ is the principal component of the

EFG tensor, and the EFG asymmetry parameter is defined as $\eta = (V_{XX} - V_{YY})/V_{ZZ}$. The (X, Y, Z) are the principal axes of the tensor, where we define $|V_{XX}| \leq |V_{YY}| \leq |V_{ZZ}|$ and note that Laplace's equation gives $V_{XX} + V_{YY} + V_{ZZ} = 0$. It follows that $0 \leq \eta \leq 1$. \mathcal{H}_{spec} will generate the vast majority of NMR spectra found in practice.

Although (2.1.5) is frequently quoted, it has the disadvantage that it assumes that the applied field is along the principal axis of the EFG tensor. Since one generally works with the field along *some* principal axis of the EFG, it is useful to generalize (2.1.5) for an arbitrarily chosen principal axis. In principal axis coordinates, the quadrupolar Hamiltonian becomes [5]

$$\mathcal{H}_Q = \frac{eQ}{2I(I+1)} \sum_{\alpha} V_{\alpha\alpha} I_{\alpha}^2. \quad (2.1.6)$$

In terms of the $V_{\alpha\alpha}$, (2.1.5) becomes in traceless form [6]

$$\mathcal{H}_{spec} = -\gamma\hbar\mathbf{I} \cdot (\hat{\mathbf{I}} + \hat{\mathbf{K}}) \cdot \mathbf{H} + \frac{eQ}{4I(2I-1)} [V_{\alpha\alpha}(3I_{\alpha}^2 - I(I+1)) + \frac{1}{2}(V_{\beta\beta} - V_{\gamma\gamma})(I_{\beta}^2 + I_{\gamma}^2)], \quad (2.1.7)$$

where α is the quantization axis and (α, β, γ) are an arbitrary permutation of (X, Y, Z) . In this form it is clear that first-order splittings will be proportional to $|V_{\alpha\alpha}|$, and the second-order splittings will be proportional to $(V_{\beta\beta} - V_{\gamma\gamma})^2$.

While (2.1.5) and (2.1.7) are useful for generating spectra, it should be noted that a number of other terms are necessary for a complete description of NMR phenomena. Some of the omissions are (a) terms to represent fixed internal hyperfine (HF) fields which may occur in ordered magnetic systems, (b) spin and orbital fluctuation terms which drive T_1 processes, (c) dipolar and indirect spin-spin coupling terms which generate T_2 processes, and (d) radiofrequency (*rf*) excitation terms. Such terms will be invoked when the need arises.

We make a number of general remarks about the use of (2.1.5) and (2.1.7) to generate and analyze spectra.

- (i) Experiments are usually carried out in one of two limiting cases, namely, $H = 0$, so that quadrupolar energies alone determine the spectrum (NQR), and secondly, the *high field limit* $\gamma H \gg \frac{e^2 q Q}{4\hbar I(2I-1)}$, wherein the quadrupolar terms may be treated with perturbation theory.
- (ii) For $I = \frac{1}{2}$ the nuclear quadrupole moment Q vanishes identically, according to the Wigner-Eckart theorem (e.g. see [6], Chap. 10).
- (iii) For nuclear spin sites with cubic symmetry, one has $V_{XX} = V_{YY} = V_{ZZ} = 0$, greatly simplifying the spectrum as with $I = \frac{1}{2}$. For quadrupolar nuclei, the effects of stray EFG's in nominally cubic structures may still play a role in the spectrum, however. Crystalline disorder caused by impurities, dislocations, etc., often cause a distribution of stray EFG's to occur at the nuclei of interest. Thus, one often finds *cubic* NMR lines with *complete first-order broadening*, so that only the $(-\frac{1}{2} \leftrightarrow \frac{1}{2})$ transition is easily resolved [20]. Such cases will be discussed as they arise.

- (iv) In the almost universally encountered high-temperature limit defined by $\hbar\gamma H \ll k_B T$, Boltzmann factors are always small compared with unity. The sign of qQ in (2.1.5) is immaterial to the spectra and is, in fact, indeterminate. For convenience, we shall always take qQ to be positive. Note also that the term “ $-I(I+1)$ ” in (2.1.5) has been inserted only to render the quadrupole tensor traceless. It plays no role in the spectral transition frequencies and may be omitted or replaced by some other quantity for calculational convenience.
- (v) In the most frequently occurring cases of non-cubic site symmetry, i.e. tetragonal or trigonal, the EFG symmetry is termed “axial”, giving $V_{XX} = V_{YY}$. Thus, $\eta = 0$ and the quadrupolar Hamiltonian is greatly simplified. We shall focus primarily on such cases and comment on how the results are affected if $\eta > 0$.
- (vi) In the high-field limit with $\eta = 0$, we comment briefly on how the EFG term affects the spectrum. If we let the angle between \mathbf{H} and the EFG principal axis Z be θ , then the simplest case is when $\theta = 0$. The eigen-energies then have the exact form $E_m = -\hbar\gamma H(1 + K)m + \hbar\nu_Q m^2/2$, where $\nu_Q = \frac{3e^2qQ}{2\hbar I(2I-1)}$, m is the $\langle I_z \rangle$ quantum number, and we have assumed a scalar shift K . In such a case, the energy levels are shifted as shown in Fig. 2.2. In the spectrum shown, the $(-\frac{1}{2} \leftrightarrow \frac{1}{2})$ transition is not affected by the ν_Q term, and the $(\pm m \leftrightarrow \pm(m+1))$ transitions are displaced by $\pm\nu_Q, \pm 2\nu_Q, \dots$, for $m = \frac{1}{2}, \frac{3}{2}, \dots$, respectively, as shown in the figure. The lines displaced by $\pm n\nu_Q$ are known as *first-order satellites*.
- (vii) For $\theta \neq 0$ the eigenfrequencies can often be estimated satisfactorily with second-order perturbation theory (see [5], Chap. VI). The first-order resonance frequencies become

$$\nu_L + \nu_{\pm n}^{(1)} = \nu_L \pm n\nu_Q(3\cos^2\theta - 1)/2, \quad (2.1.8)$$

$n = 1, 2, \dots$ Here, $n = 1$ corresponds to the $(\pm\frac{1}{2} \leftrightarrow \pm\frac{3}{2})$ transitions and $n > 1$ corresponds to transitions with progressively higher values of m . In the case of powder samples with a uniform distribution of θ over the unit sphere, the first-order quadrupole shift stated above gives rise to a *powder pattern* intensity distribution

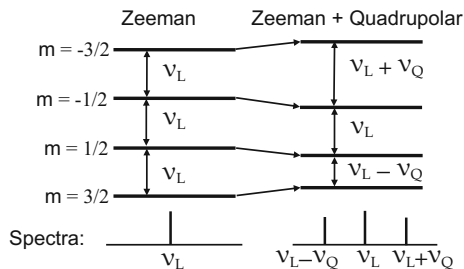


Fig. 2.2 On the left, the nuclear Zeeman term gives uniformly spaced energy levels and a single NMR line. On the right, first-order quadrupole splittings produce “first-order satellites” from the $(\pm 1/2 \leftrightarrow \pm 3/2)$ transitions. The $(-1/2 \leftrightarrow 1/2)$ transition is not affected to first order

over frequencies ranging from $\nu_L - n\nu_Q/2$ to $\nu_L + n\nu_Q/2$, where the $\theta = 0$ satellite displacement is $n\nu_Q$. The normalized distribution function is

$$\rho_q(\nu) = [6\nu_Q(\nu - \nu_L + \nu_Q/2)]^{-\frac{1}{2}}, \quad (2.1.9)$$

so that the $\theta = 0$ line at frequency $n\nu_Q$ becomes a powder pattern with a square-root singularity at $\nu = \nu_L - n\nu_Q/2$. Here, the Larmor frequency $\nu_L = \gamma H(1 + K)$. We note that m is no longer strictly a good quantum number, so there are second-order frequency shifts as well. Interestingly, the second-order frequency shifts of the satellites at $\pm n\nu_Q(3\cos^2\theta - 1)$ are equal, so that the second-order correction to their pairwise separation $2n\nu_Q(3\cos^2\theta - 1)$ vanishes. If $\eta > 0$, however, the singularities all disappear and the peak at that position becomes progressively broader as η increases.

- (viii) For the often-used $(-\frac{1}{2} \leftrightarrow \frac{1}{2})$ transition, the frequency to second order is given by

$$\nu_{\pm\frac{1}{2}}^{(2)} = \nu_L - \frac{\nu_Q^2}{16\nu_L} \left[I(I+1) - \frac{3}{4} \right] \sin^2\theta (9\cos^2\theta - 1). \quad (2.1.10)$$

In the case of a random powder sample, (2.1.8) and (2.1.10) give rise to characteristic *powder patterns* which are easy to recognize. Such a pattern is shown in Fig. 2.3, where a small amount of Gaussian broadening has been added. In cases where $\eta > 0$, these powder patterns are altered significantly. Also, if there is shift anisotropy $K(\theta)$ with a range comparable to the second-order quadrupole shift of the $(-\frac{1}{2} \leftrightarrow \frac{1}{2})$ transition, its powder-pattern shape will also be altered significantly, whereas the first-order peaks will all reflect the shift value $K(\pi/2)$. Further discussion of these effects is given below.

- (ix) When $H = 0$ we have the case of *nuclear quadrupole resonance* (NQR). The nuclear spin energies are determined entirely by Q , I , and the local EFG's. If ν_Q

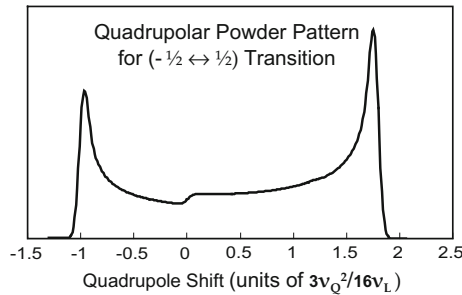


Fig. 2.3 Quadrupolar powder pattern for the $(-1/2 \leftrightarrow 1/2)$ transition based on the second-order quadrupolar energy given in 2.1.10 (axial case). Minimal Gaussian broadening has been applied. The coefficient given is for $I = 3/2$. For arbitrary half-integral I the coefficient becomes $(4I(I+1) - 3)\nu_Q^2/64\nu_L$

(see item (vi) above) is large enough, i.e. in the MHz range, then NQR spectroscopy is feasible. Considering the case of $\eta = 0$, (2.1.5) then shows that $E_{|m|+1} - E_{|m|} = (2|m| + 1)\nu_Q$. Thus, there is a series of $I - \frac{1}{2}$ NQR lines at frequencies $\nu_Q, 2\nu_Q, \dots$. The m -levels are doubly degenerate, since E_m is independent of the sign of m . The two parallel transitions produce identical signals under the usual excitation conditions [21]. If $\eta > 0$, the levels are still doubly degenerate, but the transition frequencies are now a function of η . If there are two or more NQR frequencies, their ratio can be used to determine η .

2.1.4 Definition and Interpretation of NMR Parameters: The Shift Tensor $K_{\alpha\beta}$

NMR frequency shifts are useful for characterizing a resonance line as well as analyzing different components in the magnetic susceptibility of a metallic compound. NMR shifts are useful probes, because they always reflect one or more components of magnetic polarization in the system, such as spin or Van Vleck paramagnetism. There can, of course, be magnetic polarization without a palpable NMR frequency shift, but there is no magnetic NMR shift without a source of polarization, i.e. susceptibility, to drive it. There are complications, of course, when there are fixed sources of internal magnetic polarization, such as in the *mixed state* of a type-II superconductor. Such cases are considered in Sect. 2.3. In general, we have omitted consideration of cases which involve magnetic ordering. Shifts, then, are defined to be linear in the applied magnetic field H . Analysis of shifts can be quite complex with random powder samples when the shift is anisotropic, and even more so if they are combined with inherently anisotropic quadrupolar splittings. Such cases occur frequently, and it is important to know how to analyze and characterize them.

Defining the NMR Shift

In general terms, the NMR shift is a measure of how the magnetic induction B differs at a nuclear site in a metallic specimen from its value in free space when the sample is removed. In practice, shifts are referred to bare values of the nuclear gyromagnetic ratio γ , where γ is the ratio

$$\gamma = \frac{\mu}{\hbar I} \quad (2.1.11)$$

of the nuclear magnetic moment μ to its angular momentum $\hbar I$. “Bare” values of γ are measured in compounds or other environments which are as magnetically neutral as possible. For nuclei of elements which are highly active magnetically, defining γ can be difficult and somewhat arbitrary. On the other hand, even compounds lacking a form of paramagnetism almost always have so-called chemical shifts, which are typically of the order of tens or hundreds of *ppm*. Such shifts are orbital in origin and have been discussed in detail in [6], Chap. 4.

NMR shifts in metals are typically two orders of magnitude larger than chemical shifts, so that the latter are often ignored. In high- T_c compounds, however, we shall see that, *e.g.* for ^{17}O and ^{89}Y , chemical shifts may play a role in the discussion. In d-band metals, however, the NMR shift is dominated by the spin-paramagnetic and Van Vleck terms mentioned earlier. In Sect. 2.2 we discuss a detailed formulation of these effects as well as methods for analyzing NMR shift data. Here we focus on defining and measuring the shift tensor.

Given a suitable reference γ , then, the NMR shift K is defined with respect to a change in the resonant frequency $\nu_{res} = \gamma H(1 + K)$, or

$$K = \frac{\nu_{res}}{\gamma H} - 1. \quad (2.1.12)$$

Since a lot of NMR spectroscopy is done by scanning the magnetic field, it is important to note that the fractional shift in the resonant field, which is $-K/(1 + K)$, not only has the opposite sign, but a palpably different magnitude than K if the shift is large. The unmistakable hallmark of an NMR frequency shift or of a spectrum of shifts for a powder is that they scale precisely with the applied field. If this is not the case, then one is dealing with quadrupole effects or other complications.

The NMR Shift: Tensor or Scalar?

In practice, most shifts are characterized as scalar parameters. However, formally the NMR frequency shift tensor $\mathbf{K}_{\alpha\beta}$ is defined to be the α component of the internal field at the nuclear spin divided by the β component of the applied field ([5], Chap. VI). In general, then, the induced, internal shift field is not parallel to the external field. This can be a complication in the interpretation of large shift effects. However, in cases where the shift anisotropy is 1% or less, it is a good approximation to replace the shift tensor with a scalar shift given by $K(\theta, \phi) = K_X \sin^2 \theta \cos^2 \phi + K_Y \sin^2 \theta \sin^2 \phi + K_Z \cos^2 \theta$, where the $K_{X,Y,Z}$ are the principal values of the shift tensor and (θ, ϕ) give the orientation of the field \mathbf{H} in the principal axis coordinates. Another approach, which involves no approximation, is to confine shift measurements on oriented powder or single crystal samples to field orientations along the principal axes. The (X, Y, Z) axes will generally coincide with crystalline axes of symmetry.

In metals with cubic crystal structure or with single crystals, then, shift measurements are usually straightforward. If microscopic disorder is reasonably low, then line-broadening effects will be 0.01% or less and a 1% shift can be reliably measured to good accuracy. If the nuclear site is non-cubic, however, there is the possibility of an anisotropic shift as well as the virtual certainty of quadrupolar shifts and broadening for $I > \frac{1}{2}$. For such cases it is very helpful to have either single crystals or oriented powders for non-cubic systems [40]. Otherwise, data will have to be obtained by analyzing powder patterns, *i.e.* broadened spectra which result from a sample made up of randomly oriented particles. The functional form of the axial

shift powder pattern is the same as for the first-order quadrupolar satellite pattern (2.1.9), namely,

$$\rho_K(K) = [6K_{ax}(K - K_{iso} + K_{ax}/2)]^{-\frac{1}{2}}, \quad (2.1.13)$$

where K is the shift variable, which is distributed over the range $K_{iso} - K_{ax}/2 \leq K \leq K_{iso} + K_{ax}$. For a crystal with applied field at an angle θ with respect to the axis of symmetry, the shift may be written $K_{iso} + K_{ax}(3\cos^2\theta - 1)/2$, where K_{iso} and K_{ax} are the isotropic and axial components of shift, respectively. If the three principal shift values are all different, then the symmetry is lower than axial and the singularity disappears. The distribution will have *edges* at the maximum and minimum shift values, with a peak at the intermediate principal shift value. It is possible, although it may be somewhat laborious, to extract anisotropic shifts as well as quadrupole frequency parameters from powder patterns. For the $(-\frac{1}{2} \leftrightarrow \frac{1}{2})$ transition the change of these two effects with field are opposite, so that field dependence can be employed to determine their separate values. An example of this is shown in Fig. 2.4.

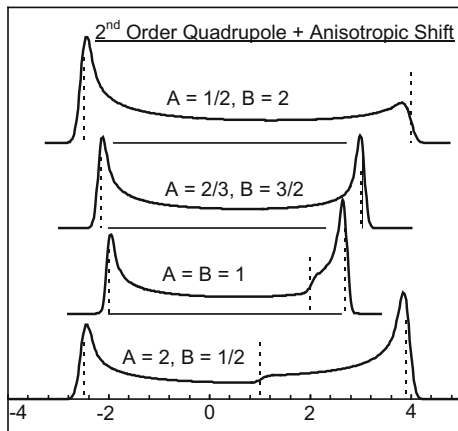


Fig. 2.4 Powder patterns for a $-\frac{1}{2} \leftrightarrow \frac{1}{2}$ transition, showing several cases of combined effects of an anisotropic shift and second-order quadrupolar broadening. The total broadening perturbation is $A \sin^2\theta (9 \cos^2\theta - 1) + B (3 \cos^2\theta - 1)$. In applied field H , $A \propto 1/H$ and $B \propto H$. In reduced units we let $B = H$, and the frequency displacement is in units of $3\nu_Q^2/16\nu_L$ (for $I = 3/2$). Plotted spectra then show the progression of powder patterns as H is varied from $1/2$ up to 2 . The dashed vertical lines show the positions of the three edges in the absence of broadening. The prominent upper singularity (see Fig. 2.4) converges with the $\theta = 0$ edge with increasing field and disappears above $B/A = 8/3$. However, there is still a visible maximum for the top example, where $B/A = 4$. Note that these spectra are actually oriented the way they would appear in a field sweep increasing to the right, and, therefore, the anisotropic shift coefficient is *negative*. With $B/A < 0$, the patterns would be quite different. Studies such as are shown here allow the practitioner to extract values of A and B from experimental data

2.1.5 Definition and Interpretation of NMR Parameters: T_1

T_1 is the time constant which describes the exchange of nuclear spin energy with the surrounding lattice, hence it is known as the *spin-lattice relaxation* time. Referring to the energy levels in Fig. 2.2, T_1 determines the rates at which nuclei make transitions between these levels. Magnetic T_1 processes are generated by fluctuating HF fields. Each magnetic HF interaction⁵ has a fluctuation spectrum with an amplitude and an autocorrelation time. The corresponding T_1 process is driven by the Fourier component of the latter spectrum at the NMR/NQR resonance frequency. The magnetic dipole T_1 processes are divided broadly into those driven by spin and orbital HF fields.

The formulation of the various relaxation processes for metallic systems including superconductors has been a major work in progress since NMR was first discovered. Below we review the interpretation of T_1 effects for simple metals and Type I superconductors (Sect. 2.2) and for d-band metals and Type-II superconductors (Sect. 2.3). The interpretation of T_1 processes for the cuprate superconductors will be discussed extensively in Chaps. 3–6. Particularly important is the role played by electron-electron interactions in T_1 phenomena. Accordingly, we review Moriya's theory of correlated electron effects in the T_1 processes of simple metals in Sect. 2.2.

Rather more rare in occurrence are quadrupolar T_1 processes generated by fluctuating components of EFG. A general theory of such effects caused by the *phonon Raman scattering process* was put forward by Van Kranendonk in the early days of NMR [30]. Such processes are extraordinarily weak, however, and have rarely been identified in metals. Nonetheless quadrupolar relaxation processes for the $^{63,65}\text{Cu}$ isotopes have occasionally been claimed to exist in solids, using the isotopic ratio of T_1 values as a diagnostic.⁶ When quadrupolar T_1 effects occur in metals, it is our conjecture that they are much more likely to be caused by ionic motion (e.g. diffusion) than by phonons.

The Magnetic Dipole Relaxation Process

Nuclear spin transitions generated by the HF interactions in (2.2.1) are known as *magnetic dipole transitions* (as opposed to electric quadrupolar transitions). Here, we analyze the magnetic dipole T_1 process in some detail. We review methods to measure it as well as certain pitfalls to be avoided in conducting such measurements. Whether measuring T_1 with high-field NMR or in zero field with NQR, the nuclear spin energy levels E_m will be labeled with the I_z quantum number m . To the extent that m is a good quantum number, the transition rate between states m and m' may be written

$$|\langle m' | I_+ | m \rangle|^2 W = |\langle m | I_- | m' \rangle|^2 W = (I - m)(I + m + 1) W \delta_{m', m+1} \quad (2.1.14)$$

⁵See Sect. 2.2 for a comprehensive definition of the magnetic HF interactions.

⁶The ratio $^{63}T_1/^{65}T_1$ is a good diagnostic for this purpose, since it is $(\gamma_{65}/\gamma_{63})^2 = 1.148$ for magnetic relaxation and is $(Q_{65}/Q_{63})^2 = 0.854$ for electric quadrupolar relaxation.

If $I = \frac{1}{2}$, then there is only a single rate W involved, where $T_1 = (2W)^{-1}$. For $I > \frac{1}{2}$ there are $2I$ rate constants and relaxation eigenmodes. The formula (2.1.14) will be correct for the cases (a) when $I = \frac{1}{2}$, (b) for arbitrary values of I when $\eta = 0$ and the field is applied along the principal axis of the EFG tensor, and (c) for NQR when $\eta = 0$. It is approximately correct for arbitrary η values when $\nu_Q \ll \gamma H/2\pi$ and for NQR when η is small. In other cases m -state mixing effects become important and it may be necessary to solve the spin Hamiltonian (2.1.5) numerically to obtain accurate matrix elements of I_{\pm} . In this discussion of T_1 analysis, we shall assume (2.1.14) to be valid, and we shall also neglect nuclear quadrupole relaxation effects. They are, as noted above, quite rare in metallic systems.

Detailed Balance in T_1 Processes

T_1 in metals is simplified by the fact that fluctuation spectra for itinerant fermions are constant over the range of typical NMR frequencies. T_1 values are therefore found to be independent of the Zeeman splitting and are the same for NMR and NQR measurements alike.⁷ We shall assume, further, that the lattice constitutes an infinite heat reservoir at equilibrium at temperature T . To illustrate the incorporation of detailed balance into the rate equations, we analyze a two-level system with energies $E_2 > E_1$, defining $\Delta E = E_2 - E_1$. The populations of these levels are designated $p_{1,2}$ and will be treated as continuous variables. The rates at which up and down transitions occur are defined to be \mathcal{W}_{21} (up) and \mathcal{W}_{12} (down), respectively. At thermal equilibrium the principle of detailed balance gives $\mathcal{W}_{21} = e^{-\beta\Delta E} \mathcal{W}_{12}$ ([6], Chap. 5) ($\beta = 1/kT$). The rate equations for populations are then

$$\frac{dp_{1,2}}{dt} = \pm[p_2\mathcal{W}_{12} - p_1\mathcal{W}_{21}], \quad (2.1.15)$$

where $p_1 + p_2 = N$ is the total number of nuclei in the ensemble. When the $p_{1,2}$ are at equilibrium we have $dp_{1,2}/dt = 0$, giving $p_2/p_1 = \mathcal{W}_{21}/\mathcal{W}_{12} = e^{-\beta\Delta E}$. Thus, the Boltzmann distribution of spin populations follows from detailed balance.

Writing $p_{1,2} = \pm\frac{1}{2}(p_2 - p_1) + N/2$, the (2.1.15) may be combined to give

$$d(p_2 - p_1)/dt = (p_2 - p_1)(\mathcal{W}_{12} + \mathcal{W}_{21}) - N(\mathcal{W}_{12} - \mathcal{W}_{21}).$$

From this relation we see that the relaxation rate of $(p_2 - p_1)$ is $(\mathcal{W}_{12} + \mathcal{W}_{21})$. Since this quantity must be independent of ΔE , we set $(\mathcal{W}_{12} + \mathcal{W}_{21}) = 2W$, where W is a rate constant which depends only on T . Detailed balance then leads immediately to

$$\mathcal{W}_{12} = \frac{2W}{(1 + e^{-\beta\Delta E})}; \quad \mathcal{W}_{21} = \frac{2We^{-\beta\Delta E}}{(1 + e^{-\beta\Delta E})}. \quad (2.1.16)$$

Using (2.1.16), (2.1.15) then becomes

⁷Note, however, that NMR and NQR reflect different relaxation modes, as will be seen below. For example, if $I = \frac{3}{2}$, for NMR $1/T_1 = 2W$, whereas the single rate measured with NQR is $6W$, or one-third the length of the conventionally defined T_1 .

$$\frac{dp_{1,2}}{dt} = -2W \left[p_{1,2} - \frac{N e^{-\beta E_{1,2}}}{\sum_i e^{-\beta E_i}} \right]. \quad (2.1.17)$$

Even though p_1 and p_2 appear to act independently, they are not, of course, independent. The general solution to (2.1.17) is seen to be

$$p_{1,2}(t) = (p_{1,2}(0) - p_{01,02})e^{-2Wt} + p_{01,02}, \quad (2.1.18)$$

where $p_{01,02} = N \exp(-\beta E_{1,2}) / \sum_i \exp(-\beta E_i)$ are the equilibrium population values. This result also satisfies $p_1(t) + p_2(t) = N$ if $p_1(0) + p_2(0) = N$, which must be the case.

Relaxation Equations for $I > \frac{1}{2}$

Generalization of the foregoing result to multi-level nuclear relaxation equations is straightforward. They can always be written in terms of the *difference* variables

$$d_m = p_m - p_{0m}, \quad \text{with } p_{0m} = N \exp(-\beta E_m) / \sum_m \exp(-\beta E_m), \quad (2.1.19)$$

where m is the quantum number for the energy eigenvalues. We note that the value of p_{0m} does not depend on the choice of the zero-point of energy. In general, then, one can measure T_1 by creating a non-equilibrium population distribution, then observing the decay toward equilibrium of the population difference of some suitable pair of levels using spin-echo excitation. The latter pair must be chosen to have $|\Delta m| = 1$ for magnetic excitation, and they must be chosen to reflect a non-equilibrium population difference during the equilibration process.

If the initial non-equilibrium condition is created by applying an *rf* pulse to some pair of levels, note that the recovery can often be observed using spin-echo signals from a *different* pair of levels.⁸ This degree of experimental freedom is not often used in NMR. It could be used, for example, to avoid multiple echo effects in a T_1 measurement when T_1 is very short.

Relaxation Eigenmodes for $I > \frac{1}{2}$

For multi-level nuclear spin Hamiltonians ($I > \frac{1}{2}$) [42] there is an eigenmode structure to the relaxation equations with multiple relaxation eigenrates. We illustrate this situation with the simple example of $I = \frac{3}{2}$, for which there are four energy levels as shown in Fig. 2.2. The dynamical equations for the differences d_m are then

⁸This requires the ability to be able to apply *rf* pulses to the sample at two separate frequencies, which can be a very useful adjunct to the usual spectrometer setup.

$$\frac{dd_{3/2}}{dt} = -3Wd_{3/2} + 3Wd_{1/2} \quad (2.1.20a)$$

$$\frac{dd_{1/2}}{dt} = 3Wd_{3/2} - 7Wd_{1/2} + 4Wd_{-1/2} \quad (2.1.20b)$$

$$\frac{dd_{-1/2}}{dt} = 4Wd_{1/2} - 7Wd_{-1/2} + 3Wd_{-3/2} \quad (2.1.20c)$$

$$\frac{dd_{-3/2}}{dt} = 3Wd_{-1/2} - 3Wd_{-3/2} \quad (2.1.20d)$$

We seek solutions of the form $d_m = c_m \exp(-\lambda Wt)$. Substitution into (2.1.20) then yields the matrix equation

$$\begin{bmatrix} \lambda - 3 & 3 & 0 & 0 \\ 3 & \lambda - 7 & 4 & 0 \\ 0 & 4 & \lambda - 7 & 3 \\ 0 & 0 & 3 & \lambda - 3 \end{bmatrix} \begin{bmatrix} c_{3/2} \\ c_{1/2} \\ c_{-1/2} \\ c_{-3/2} \end{bmatrix} = \begin{bmatrix} 0 \\ 0 \\ 0 \\ 0 \end{bmatrix}$$

This matrix is solved straightforwardly. The characteristic equation is

$$\lambda^4 - 20\lambda^3 + 108\lambda^2 - 144\lambda = 0, \quad (2.1.21)$$

for which the solutions are $\lambda = (0, 2, 6, 12)$. The corresponding decay rates are $\lambda_0 = 0$, $\lambda_2 = 2W = T_1^{-1}$, $\lambda_6 = 6W = 3T_1^{-1}$, and $\lambda_{12} = 12W = 6T_1^{-1}$. Ignoring the null mode, the corresponding eigenvectors for T_1 , $T_1/3$ and $T_1/6$ may be written $\{3, 1, -1, -3\}$, $\{-1, 1, 1, -1\}$, and $\{-1/3, 1, -1, 1/3\}$, respectively.

The solutions to (2.1.20) may be applied to different techniques for measuring T_1 . We illustrate their use in the simple case of a cubic environment where $E_m = -\hbar\gamma_n(1 + K)Hm$. Since $|E_m| \ll k_B T$, we may write (2.1.19) $p_{0m} \approx \frac{N}{2I+1}(1 - \delta m)$, where $\delta = \hbar\gamma_n H(1 + K)\beta$. Then if we apply an *rf* pulse with pulse-angle θ to the spins, the resulting initial condition is

$$p_m(0) \approx \frac{N}{2I+1}(1 - \delta \cos \theta m).$$

As a result, the initial values are $d_m(0) \approx \frac{N}{2I+1}(1 - \cos \theta)m$. The $d_m(0)$ have the form $\{3, 1, -1, -3\}$ of the “ T_1 ” mode, so that the solution can be written

$$d_m(t) \approx \frac{Nm\delta}{2I+1}(1 - \cos \theta)e^{-t/T_1}.$$

If $\theta = \pi$, then one has a perfect *inversion*, which gives the largest excursion in signal amplitude. The time variation of the spin echo signal is then proportional to

$$p_m(t) - p_{m+1}(t) = \frac{N\delta}{2I+1} [1 - (1 - \cos \theta) e^{-t/T_1}]. \quad (2.1.22)$$

If $p_m(0) = p_{m+1}(0)$ for all applicable m , then we have a condition known as *saturation*, which also yields a single-exponential recovery $\propto (1 - \exp(-t/T_1))$.

Recovery Mode When Only the $(-\frac{1}{2} \leftrightarrow \frac{1}{2})$ Transition is Excited

If there are quadrupolar splittings, then a single pulse applied to the $(-\frac{1}{2} \leftrightarrow \frac{1}{2})$ transition results in a $\{d_m(0)\}$ vector with the form $a_0\{0, 1, -1, 0\}$. Writing the decay mode as a superposition of the foregoing eigenmodes, we have

$$\{d_m(t)\} = \frac{1}{10} a_0 [\{3, 1, -1, -3\} \exp^{-t/T_1} + 9\{-1/3, 1, -1, 1/3\} \exp^{-6t/T_1}].$$

The spin echo signal for the $(-\frac{1}{2} \leftrightarrow \frac{1}{2})$ transition will therefore exhibit the well-known decay function

$$E(t) = E_0 (0.9 \exp^{-6t/T_1} + 0.1 \exp^{-t/T_1}). \quad (2.1.23)$$

Such a precise mathematical form occurs only for excitation of a single pair of levels over a time interval which is short compared with $T_1/6$. If relaxation begins to take place during the initial excitation phase, then the simple form of the initial condition is lost and the decay will be rather more complicated. In the foregoing example, $d_{3/2}(t)$ would be proportional to $(\exp -t/T_1 - \exp -6t/T_1)$, so that it would deviate very quickly from its initial value of zero. As we noted earlier, the relaxation measurement could be conducted in this fashion, i.e. by monitoring a different transition frequency from the one used for the initial excitation.

The T_1 analysis described here for $I = \frac{3}{2}$ is straightforwardly extended to larger (half-integer) values of I . There will be $2I + 1$ equations such as the (2.1.20) above, so the solutions will have added complexity. But solving the determinants for $I > \frac{3}{2}$ is simplified by the fact that as increments of 1 are added to I , the eigenvalues for the previous case are carried forward.

The NQR Case

Continuing our discussion of an $I = \frac{3}{2}$ nucleus, we consider finally the NQR case, where the $\pm\frac{1}{2}$ levels and the $\pm\frac{3}{2}$ levels are degenerate pairs separated by an energy difference of $h\nu_{NQR} = h\nu_Q(1 + \eta^2/3)^{1/2}$. A single excitation pulse at the NQR frequency then creates an initial condition given by $\{d_m\} = a_0\{-1, 1, 1, -1\}$. This effectively 2-level system relaxes entirely via the *symmetric mode* with a single decay rate $3/T_1$. One must be careful to take account of the relaxation mode effects when comparing T_1 data obtained with different methods.

We make a few additional remarks about the decay mode effects described above for the $I = \frac{3}{2}$ system. First, there are many nominally cubic systems where the observed signal is dominated by the $(-1/2 \leftrightarrow 1/2)$ transition, because transitions to higher m -values are broadened by stray first-order quadrupolar splittings. Such

splittings are the consequence of impurities and other forms of crystalline disorder. If such broadening is severe, magnetization recovery may take place via (2.1.5) rather than with the expected single-exponential T_1 decay. Since there is a dramatic difference between these two cases, it is very important to be aware of such broadening effects.

A second point we wish to emphasize is that the analysis of T_1 relaxation curves given here for $I = \frac{3}{2}$ is entirely independent of the nature of the NMR spectrum. The functional behavior depends only on which pair of levels is used to excite a non-equilibrium initial condition, and on the fact that the quantum numbers $m = \langle I_z \rangle$ are relatively pure in characterizing the energy eigenstates. If the latter condition is not fulfilled, then numerically evaluated eigenfunctions may be needed to generate sufficiently accurate relaxation rates.

Measuring T_1 in the Presence of Spectral Diffusion

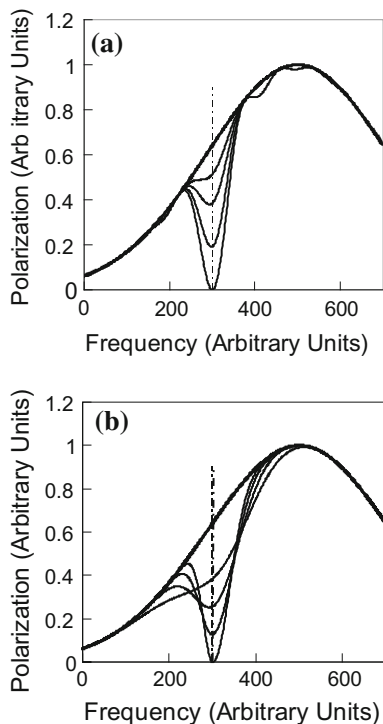
We consider briefly some well-known problems encountered in T_1 measurements. Two of the most troublesome are the related problems of inhomogeneous broadening and spectral diffusion. These problems occur frequently in d-band metals and intermetallic compounds. The key to accurate T_1 measurements is the experimenter's ability to create a strongly non-equilibrium population difference between a pair of nuclear energy levels as an initial condition. The T_1 recovery will then be accompanied by a spin-echo signal which undergoes a substantial change in amplitude. In cases of severe inhomogeneous broadening such as that shown in Fig. 2.5, a difficulty arises from the fact that a single pulse of rf field will only affect a region of width γH_1 , where H_1 is the amplitude of the rf pulse field. The narrow region saturated by a single pulse is shown as a dotted line in Fig. 2.5a. If the broadening is entirely static, it may be possible to focus the measurement on the polarization behavior at precisely the irradiation frequency, i.e. the center frequency of the population disturbance shown in the figure. As noted in Sect. 1.2.2, this can be done by carefully integrating the entire area under the spin echo, so that the measured recovery curve will accurately reflect what is taking place at $\omega = \omega_{rf}$.

However, such broadening may actually have a partially dynamical character owing to the presence of spin-spin couplings of the form

$$\mathcal{H}_{ff} = BI_{i\pm}I_{j\mp} \quad (2.1.24)$$

between neighboring nuclei. Under circumstances which occur frequently, the \mathcal{H}_{ff} interactions lead to *flip-flop* dynamic processes between neighboring spins, which then leads to a rapid smearing of the band of excited spins over a much wider range of frequencies than those excited directly by the rf pulse(s). This process, known as *spectral diffusion*, is illustrated with dashed lines in Fig. 2.5b. There results what appears to be a rapid recovery of the polarization at the excitation frequency. However, such a recovery has nothing to do with the T_1 process, but is easily mistaken for it. Often it is much faster than T_1 , and results in the experimenter's inability to achieve inversion of the polarization [43]. This highly undesirable effect has been known in adverse cases to render T_1 measurements unfeasible.

Fig. 2.5 **a** The saturation effect of a $\pi/2$ pulse applied at frequency ω_0 is shown for an effective pulse field amplitude of 20 in units of the frequency scale. The polarization curve is also shown at several later times as T_1 recovery takes place *without spectral diffusion*. **b** Development with time of the polarization curve is shown at several stages following the same initial saturation pulse as in (a). The curves are a Gaussian model in which there is no T_1 recovery effect, thus the total polarization, plus its first moment $\int (\omega - \omega_0) P(\omega) d\omega$, are conserved over the time interval shown. Note the spurious “recovery” of the polarization at frequency ω_0 as a function of time



We consider here the circumstances which give rise to spectral diffusion effects and offer a few suggestions on how to deal with this problem. The flip-flop process $(m, m') \rightarrow (m \pm 1, m' \mp 1)$ between (primarily) nearest-neighbor (nn) spins has been recognized since the early days of NMR as essential for spin diffusion, as well as for maintaining thermal equilibrium within the nuclear spin system. Spectral diffusion is, in fact, a process whereby a disturbance in a narrow frequency range is able to diffuse over the entire NMR line so as to create a *uniform spin temperature*. However, since an energy-conserving flip-flop transition can only take place between neighbors with nominally the same Larmor frequency, i.e. the same shift value, it is interesting to consider how polarization can migrate over large frequency intervals such as depicted in Fig. 2.5b. With coupling energy of the form of (2.1.24), it is plausible that a flip-flop transition could take place between neighboring spins with a Zeeman frequency mismatch of the order of $\Delta\omega \sim B$ and still conserve energy, the difference in Zeeman energies being taken up by the transverse terms and eventually dissipated by other flip-flop processes. Over a large number of such fluctuations, the narrow polarization disturbance created by an rf pulse could broaden symmetrically over frequencies well beyond the confines of the initial excitation profile. To have this happen, of course, the inhomogeneous broadening must be local in character and be otherwise configured to facilitate the process.

One method for measuring T_1 under these circumstances is to endeavor to saturate the entire line with a string of pulses known as a *comb* instead of a single pulse. Were this possible, then all polarization variables would relax back to equilibrium with the single time constant T_1 . If pulses at a single frequency do not produce the desired saturation effect, then applying frequency modulation to cover the entire resonance line is known to be effective [44]. At low temperatures, however, long strings of pulses may produce undesirable heating effects. If T_1 is long enough, another more exotic (but widely used) method is to use *field switching* to create a non-equilibrium initial condition for the T_1 measurement. The field at the sample can be switched mechanically or electronically.

The most obdurate cases occur when T_1 is too short, even at low temperatures, for field switching, and pulse combs are also not feasible. One's only option may be to hope that spectral diffusion will run its course in a time less than T_1 , and that the final stage of the polarization recovery process can be analyzed to extract the T_1 rate. Needless to say, such an approach also has limited applicability.

2.2 NMR Probe of sp-Band Metals and Type I Superconductors

In order to put high- T_c materials into context, this section gives as background material a brief summary of the basic static and dynamic magnetism of “simple” metals as sensed by the NMR probe. These systems give a historical perspective of the subject and provide foundation for the treatment of the more complex d-electron metals. In typical *good* metals we think about electrons as itinerant fermions which occupy Bloch wavefunctions $u_k(\mathbf{r})e^{ik\cdot\mathbf{r}}$. Such orbitals are often far removed in character from the atomic states they are actually composed of. Calculations of NMR shift, relaxation, and indirect spin-spin couplings in metals were originally formulated in this band-theoretical language. The s-character of band electrons is always present and often plays a major role. In contrast, high- T_c systems are *bad metals*, often with just enough mobile carriers to render the *d*-holes on the Cu^{2+} sites itinerant. Some properties remain atomic-like in character and can be thought of usefully in terms of localized wavefunctions. Perhaps by accident, there is very little *s*-character in the wavefunctions of most high- T_c ions, allowing the less familiar *p* and *d* orbitals to dominate.

In this section we review the energy-band, k-space picture used to describe the static and dynamic magnetism sensed by the NMR probe in both the *normal* (non-superconducting) and *superconducting* (SC) states. We begin the discussion with the idealized Korringa treatment of NMR shifts and relaxation, then discuss important modifications of this picture for actual sp-band metals.

Historically, the first NMR studies of superconductivity were done on this class of materials. We review problems encountered in reconciling both the shift and relaxation behavior with the BCS theory [39] for these systems. It was with elemental metals such as Hg, Sn, Pb, and Al that questions such as that of the role played by spin-orbit coupling in the behavior of the spin susceptibility and corresponding NMR

(Knight) shift first came to light. They also gave us our first clear understanding of the BCS coherence peak in the T_1 rate [64].

Since even before the BCS theory of superconductivity [39] was announced, NMR shifts have been employed to investigate the nature of the superconducting state. In the early days the only known metallic NMR shift was the *s-contact Knight* shift. Moreover, the original BCS ground state was an eigenfunction of S_z , leading to the naive expectation that $K(T) \propto \chi_{spin}(T)$. The actual reality was rather more complex. This interesting piece of NMR history will be touched upon in Sect. 1.2. Measurement of such effects has become a standard application for NMR studies. Observation of shift behavior is also very important in the study of high- T_c systems and for any of the latter-day unconventional superconductors.

2.2.1 NMR Shifts and Relaxation in Simple Pauli Paramagnets

Following on the discovery of the s-contact NMR shift by Knight [32], one of the first theoretical milestones for the NMR study of metals was the Korringa relation between the latter shift and the product $T_1 T$, which was also shown to be independent of temperature [41]. These results were expected to apply to cubic sp-band metals, where it is noteworthy that the p-electrons with their far smaller HF couplings have a nearly negligible effect on both the NMR shift and T_1 . The surprise of substantial deviations from the Korringa relation for simple systems such as the alkali metals were therefore a stimulus for Moriya's treatment of electron-electron interactions in these systems. The result was important modifications to the Korringa relation which were verified experimentally. This was a very important step in the treatment and understanding of electron interactions in metals. We review these developments in the following subsections.

The Comprehensive HF Coupling Hamiltonian in Solids

As a preliminary step we introduce here the comprehensive HF Hamiltonian

$$\mathcal{H}_{HF} = 2\gamma\hbar\mu_B\mathbf{I} \cdot \left[\frac{\mathbf{I}}{r^3} - \frac{\mathbf{s}}{r^3} + \frac{3\mathbf{r}(\mathbf{s} \cdot \mathbf{r})}{r^5} + \frac{8}{3}\pi s\delta(\mathbf{r}) \right], \quad (2.2.1)$$

where $\gamma\hbar\mathbf{I}$ is the nuclear moment located at $\mathbf{r} = 0$ and \mathbf{I} and \mathbf{s} are the orbital and spin angular momentum operators, respectively, of an itinerant fermion located at \mathbf{r} (see [5], Chap. VI). Equation (2.2.1) can be written $-\gamma\hbar\mathbf{I} \cdot \mathbf{H}_e$, where \mathbf{H}_e is an effective HF-field operator which is the ultimate source of all magnetic shift and relaxation effects in the metallic environment. There are three distinct types of interactions, namely the orbital field, the dipolar field, and the s-contact interaction. Although it took a number of years for them to emerge, calculations for the metallic shifts listed above were all ultimately based on (2.2.1). Evaluating the thermally averaged effects

of H_e in metallic systems is a matter of great subtlety and complexity. In a very real sense, this is the essence of the *high- T_c problem* for the NMR probe.

The Knight Shift: s-contact HF Coupling in an sp -Band Metal

The so-called s-contact HF field and its corresponding NMR shift in copper metal were discovered by Knight [32]. This shift is simply given by the expectation value of the final term of (2.2.1) when spin polarization from an external field H is present. There results a temperature-independent NMR shift given by

$$K_s = \alpha_s \chi_{sp}, \quad (2.2.2)$$

where $\alpha_s = \frac{8\pi}{3} \langle |u_k(0)|^2 \rangle$, $\langle \rangle$ indicating an average over the Fermi surface. $\chi_{sp} = \frac{1}{2} (g\mu_B)^2 n(E_F)$ is the spin susceptibility of the sp band, where $n(E_F)$ is the Fermi surface density of states per atom for one direction of spin [75]. We also note that the dipolar HF coupling, i.e. the second and third terms of (2.2.1), also yields a palpable NMR shift in many cases. It vanishes at sites having cubic symmetry, and is typically an order of magnitude or so smaller than the contact shift. In high- T_c materials, where contact shifts are often absent, the dipolar terms take on a much greater significance than for cubic metals.

Interestingly for the case of copper metal, it later developed that some 40% of the orbital character of the Fermi surface is d-like [33]. As a result, a significant fraction of the observed Knight shift for copper is attributable to the orbital Van Vleck term discussed in the next subsection [34].

The Korringa Calculation of T_1

The idealized viewpoint regarding a simple metal is epitomized by the seminal calculation of NMR shift and relaxation time by Korringa [41]. In this case, noninteracting electrons were assumed, with a density of states at the Fermi surface describable by band theory. HF interactions with the relevant nuclear spins were limited, not unreasonably, to the s -contact interaction (2.2.1), the p -electron dipolar coupling being negligibly weak in comparison. Cubic symmetry allowed quadrupolar effects and p -electron contributions to the NMR shift to be ignored, and any gradient to the density of states deemed too small to alter low-temperature behavior. The shift expression is given above in (2.2.2).

Next, we need to develop an expression for T_1 at the same level of approximation. We use the basic *golden rule* expression from time-dependent perturbation theory, where the perturbing interaction is the s -contact term from (2.2.1), $\mathcal{H}_{sc} = -\frac{8\pi}{3} \hbar^2 \gamma_n \gamma_e \delta(\mathbf{r}) \mathbf{I} \cdot \mathbf{s}$. If we consider the elemental transition from state $|\mathbf{k} \uparrow m\rangle$ to state $|\mathbf{k}' \downarrow m+1\rangle$, where m is the initial nuclear spin quantum number, the rate for such a transition may be written [6]

$$\mathcal{W}_{\mathbf{k}' \downarrow m+1, \mathbf{k} \uparrow m} = \frac{2\pi}{\hbar} |\langle \mathbf{k}' \uparrow m+1 | \mathcal{H}_{sc} | \mathbf{k} \downarrow m \rangle|^2 \delta(E_k - E_{k'}). \quad (2.2.3)$$

To complete the calculation this transition rate must be summed over initial electron states $|\mathbf{k} \uparrow\rangle$ which are occupied and final states $|\mathbf{k}' \downarrow\rangle$ which are unoccupied.

The operative term in \mathcal{H}_{sc} is the one $\propto I_+ S_-$, whereupon the squared matrix element becomes

$$|\langle \mathbf{k} \uparrow m | \mathcal{H}_{sc} | \mathbf{k}' \downarrow m+1 \rangle|^2 = \left[\frac{4\pi}{3} \gamma_n \gamma_e \hbar^2 |u_{\mathbf{k}}(0) u_{\mathbf{k}'}(0)| \right]^2 (I-m)(I+m+1). \quad (2.2.4)$$

The principal approximation is to assume that all states in the vicinity of the Fermi surface have approximately the same probability density at the nucleus. Thus, we may replace the quantity $|u_{\mathbf{k}}(0) u_{\mathbf{k}'}(0)|^2$ with the squared Fermi surface average $\langle |u_{\mathbf{k}}(0)|^2 \rangle^2$. Introducing the restricted sums on \mathbf{k} and \mathbf{k}' and noting further that $1/T_1$ is twice the coefficient of $(I-m)(I+m+1)$ (see Eq. (2.1.14)), this gives [63]

$$1/T_1 = \frac{4\pi}{\hbar} \left[\frac{4\pi}{3} \gamma_n \gamma_e \hbar^2 \langle |u_{\mathbf{k}}(0)|^2 \rangle \right]^2 \sum_{\mathbf{k}, \mathbf{k}'}^{(r)} \delta(E_{\mathbf{k}} - E_{\mathbf{k}'}). \quad (2.2.5)$$

The restricted sums $\sum_{\mathbf{k}, \mathbf{k}'}^{(r)}$ can be replaced with energy integrals where, for example, the sum on \mathbf{k} of states with energy E becomes $\int n(E) dE$, where $n(E)$ is the density of states, and the occupation restriction is enforced with the Fermi occupation function $f(E) = [\exp \beta(E - E_F) + 1]^{-1}$.

The summation in (2.2.5) then becomes

$$\int dE \int dE' n(E) n(E') f(E) (1 - f(E')) \delta(E - E') = \int n(E)^2 f(E) (1 - f(E)) dE. \quad (2.2.6)$$

The final step is to note that the function $f(E)(1 - f(E))$ is very sharply peaked at E_F at the usual experimental temperatures, so that $n(E)^2$ can be replaced with $n(E_F)^2$. Then we note that the area under the peak in $f(E)(1 - f(E))$ is easily shown to be $k_B T$. The relaxation rate becomes

$$1/T_1 = \frac{4\pi k_B T}{\hbar} \left[\frac{4\pi}{3} \gamma_n \gamma_e \hbar^2 \langle |u_{\mathbf{k}}(0)|^2 \rangle \right]^2 n(E_F)^2. \quad (2.2.7)$$

This expression may be combined with the result in (2.2.2) to give the *Korringa product*, which we write as

$$\frac{1}{T_1 T K_s^2} = \frac{4\pi k_B \gamma_n^2}{\hbar \gamma_e^2}. \quad (2.2.8)$$

Equation (2.2.8) suggests that $1/T_1 T$ divided by K_s^2 for these kinds of metals should equal an expression made up of physical constants which is independent of the other properties of the metal. As we shall see below, the result of Moriya's theory is to multiply the right-hand side of (2.2.8) by a constant factor < 1 . Setting that aside for the moment, however, let us see how well the Korringa relation is obeyed

in simple metals. In Table 2.1 shift and relaxation data from the literature are listed for the alkali metals and the noble metals Cu, Ag, and Au [7].

These elemental metals all have cubic crystal structures, so that dipolar shift effects do not come into play. Using the measured shift values, values of $T_1 T$ extracted from (2.2.8) are compared with experimental values. It is seen that the latter values are generally smaller than those obtained from (2.2.8). Including p -electron dipolar hyperfine fields in the relaxation calculation would only make this discrepancy larger. Thus, the most serious defect in the Korringa treatment appears to be the neglect of electron-electron exchange enhancement effects, which we shall discuss next.

2.2.2 The Moriya Theory of Exchange Enhancement in Simple Metals

There are various corrections one could make to the Korringa treatment of relaxation. The electron-electron interaction potential has the effect of enhancing the spin susceptibility, and thus the NMR shift [57], in close analogy with the enhancement effect of ferromagnetic exchange among localized moments. However, it was pointed out by Moriya [58] that exchange fluctuations would also enhance the T_1 process. Moriya's calculation of this effect in the *random phase approximation* showed this enhancement effect to be substantial, but not as great as that of the shift and susceptibility. This is consistent with the values shown in Table 2.1, where the experimental Korringa product (Relative Korr. Prod.) is consistently smaller than the result in (2.2.8). Thus, the measured Korringa products can be used with the Moriya theory to estimate the magnitude of these enhancement effects (see below).

We give an outline of the random-phase approximation calculation here, and refer the interested reader to Refs. [7, 58] for a more detailed account. As noted

Table 2.1 NMR shift and relaxation data are tabulated for alkali metals and for the noble metals, along with values of $T_1 T$ derived from (2.2.8) from the compilation by Narath [7]. To test the validity of the Korringa relation, a relative Korringa product defined as $(T_1 T K_s^2)^{-1}$ divided by $4\pi k_B \gamma_n^2 / \hbar \gamma_e^2$ is listed in column five

Metal and isotope	$K_s(\%)$	$T_1 T$ (expt.) (s K)	$T_1 T$ (Korringa) (s K)	Relative Korr. Prod.
^7Li	0.0263	45.0 ± 2	26.0	0.58
^{23}Na	0.112	4.8 ± 0.1	3.1	0.65
^{85}Rb	0.650	0.81 ± 0.08	0.63	0.78
^{133}Cs	1.47	0.13 ± 0.01	0.069	0.53
^{63}Cu	0.232	0.9 ± 0.2	0.7	0.78
^{109}Ag	0.522	9.0 ± 1.0	4.5	0.50
^{197}Au	1.4	4.0 ± 0.5	4.5	1.13

Table 2.2 A tabulation of enhancement parameters α derived for a selection of s-band metals from experimental data using (2.2.9). For comparison, calculated values given by Pines [57] are listed

Elemental metal	α from $\mathcal{K}(\alpha)$	α calc. (Pines)
${}^7\text{Li}$	0.36	0.37
${}^{23}\text{Na}$	0.30	0.24
${}^{85}\text{Rb}$	0.19	0.15
${}^{109}\text{Ag}$	0.43	0.32

above, the shift has a simple exchange-enhancement factor, $K_s = K_{s0}/(1 - \alpha) = \alpha_s \chi_{s0}/(1 - \alpha)$, where $\alpha = \rho_0 \chi_{s0}$, and $\rho_0 = 2\pi\zeta/\hbar^2\gamma_e^2$. Finally, ζ is the q -independent (by assumption) electron-electron interaction potential. The single parameter ζ drives the enhancement of both static and dynamic spin susceptibilities in the random phase approximation picture. For T_1 the fluctuation enhancement is q -dependent. In Sect. 3.5 these magnetic properties will be discussed in terms of q and ω -dependent susceptibilities. Here, we simply state the result for a spherical Fermi surface:

$$\frac{1}{T_1 T K_s^2} = \frac{4\pi k_B \gamma_n^2}{\hbar \gamma_e^2} \mathcal{K}(\alpha), \quad (2.2.9)$$

where $\mathcal{K}(\alpha) = 2(1 - \alpha)^2 \int_0^1 dx x/[1 - \alpha G(x)]^2$. Here $G(x)$ is the Lindhard function for free electrons given by $\frac{1}{2}\{1 + [(1 - x^2)/2x]\ln|(1 + x)/(1 - x)|\}$, with $x = q/2k_F$. $G(x)$ is integrated over the range of q values which span the Fermi surface. We see in (2.2.9) that the Korringa product of (2.2.8) is simply multiplied by the quantity $\mathcal{K}(\alpha)$. The enhancement factor for K_s is that for $q = 0$ ($G(0) = 1$), while that for $1/T_1$ is for $|q| > 0$ ($G(|q| > 0) < 1$). Therefore, $\mathcal{K}(\alpha)$ declines from 1 to 0 as α varies from 0 to 1 [61].

If other effects which modify the Korringa product are largely absent [62], the experimental value of $\mathcal{K}(\alpha)$ can be used to estimate the electron-electron exchange (i.e. the value of α) in *sp*-band metals. A few examples are given in Table 2.2, where α values in the range of $0.2 \leq \alpha \leq 0.4$ are seen to be typical. Rather surprisingly, susceptibility enhancement effects are present to the degree of 25% to more than 50% in these *nearly free-electron metals*. The Korringa product is often used as a diagnostic tool to examine the nature of the T_1 process.

2.2.3 NMR in the Superconducting State of Simple Metals

We present here a brief account of the superconducting properties of *sp*-band metals. Historically, several fundamental issues were resolved with these systems following initial uncertainties regarding both theory and experiment. A clear and comprehensive review of early work was given by MacLaughlin [9]. Some elemental metals

addressed in the early days were Hg(4.15K), β Sn(3.74K), Pb(7.22K), and Al(1.18K), where their respective values of T_c are given in parentheses. They are all Type I superconductors, which means that their coherence lengths $\xi(0)$ are long compared with their London penetration depths $\lambda(0)$ [60].

With the announcement of BCS theory [39], there were a number of interesting issues to investigate. The principal ones for the NMR probe were (a) the expected collapse of the spin susceptibility at $T < T_c$ owing to the SC energy gap for quasiparticle excitations and (b) the existence of a singularity, which becomes the *coherence peak*, just below T_c in a plot of $1/T_1$ versus T . Because of the large superconducting diamagnetism which occurs below T_c , virtually the only means of measuring the relatively tiny Pauli susceptibility term is through the associated Knight shift K_s (Eq. 2.2.2). We shall discuss the superconducting shift measurements first.

The Knight Shift for $T < T_c$: Verifying the Yosida Function

Performing NMR measurements in the SC state of Type I superconductors was a particular experimental challenge, because of the limited magnetic field penetration depth $\lambda \sim 500 \text{ \AA}$ for these systems. In order to get a reasonably uniform internal field for NMR studies, experiments were performed on fine particles or thin films with at least one dimension which was small compared with λ . The resulting samples generally exhibited superconductivity with T_c near the bulk value and NMR lines with relatively little diamagnetic shift or inhomogeneous broadening. Particles with dimension $d \ll \lambda$ have greatly reduced diamagnetism in the SC state. Other than that, it was generally believed that these samples exhibited *bulk NMR properties*.

However, the peculiar results obtained at first for $K(T)$ versus T for $T < T_c$ demonstrated that the foregoing statements were not entirely correct. To see this clearly, we must first describe the results that were expected from the shift measurements, then what was actually found, and finally, how to account for the observed data. The BCS theory prescribed an energy gap $\Delta(T)$ above the superconducting ground state for quasi-particle excitations when $T < T_c$. As $\Delta(T)$ increases below T_c the spin susceptibility $\chi_{sp}(T)$ and $K_s(T) = \alpha_s \chi_{sp}(T)$ were expected to decline and asymptotically approach 0 as $T \rightarrow 0$. The theoretical functional form of $\chi_{sp}(T)$ for $T < T_c$ is known as the Yosida function [49].

Experimentally, however, large residual $T \rightarrow 0$ shift values were reported. For the ^{199}Hg NMR in SC Hg, for example, $K_s(T \rightarrow 0)/K(T > T_c) \simeq 2/3$ was found [48], with similar results for ^{119}Sn in βSn [59], ^{207}Pb in Pb [45], and ^{27}Al in Al [47]. These results caused great consternation and confusion, and it was a number of years before a satisfactory understanding was reached [50].

Spin-Orbit Scattering: The Ferrell–Anderson Picture

In the end, it was realized that the theoretical preparation was incomplete, and further developments with the Al metal samples showed that the earliest results were incorrect. We shall return to the Al story below. The problem with the Yosida/BCS calculation was that it had neglected spin-orbit coupling and its role in generating spin-flip scattering processes. The situation was eventually addressed and for the most part resolved in short papers by Ferrell [51] and Anderson [52], as well as in a longer paper by Abrikosov and Gorkov [53].

We consider briefly the physical picture presented in Anderson's treatment [52]. In the presence of spin-orbit coupling one must bear in mind that $\langle S_z \rangle$ for the electrons is no longer a good quantum number, and that the spin-up and spin-down states are mixed into eigenstates which no longer have any particular average value of spin. However, a very subtle point is this: In *clean, bulk regions of the pure metal* there is no spin-flip scattering even in the presence of strong spin-orbit coupling. Thus, the spin susceptibility will still vanish as $T \rightarrow 0$ in the SC state. However, what modifies this ideal result is a spin-flip scattering lifetime τ_{so} which is short enough that the quantity $\hbar/\Delta(0)\tau_{so}$ is no longer small. In other words the smearing of the eigenstate energies from τ_{so} becomes comparable with the SC energy gap. Spin-flip scattering occurs only where ordinary potential scattering is strong, e.g. near surfaces and near impurities in the bulk. Ironically, then, this effect will be important near surfaces where *rf* fields penetrate and NMR signals are excited, but not necessarily in bulk regions which cannot be probed.

Anderson treated the spin-orbit scattering problem using his theory of *dirty superconductors* [54]. His result for the $T \rightarrow 0$ susceptibility ratio is an expression which can be integrated numerically, from which the following limiting cases are given [52]:

$$\frac{\chi_{so}(T \ll T_c)}{\chi_{so}(T > T_c)} \approx \frac{1}{6} \frac{\hbar}{\Delta(0)\tau_{so}}, \quad \Delta(0) \gg \hbar/\tau_{so} \quad (2.2.10a)$$

$$\frac{\chi_{so}(T \ll T_c)}{\chi_{so}(T > T_c)} \approx 1 - 2 \frac{\Delta(0)\tau_{so}}{\hbar}, \quad \Delta(0) \ll \hbar/\tau_{so}. \quad (2.2.10b)$$

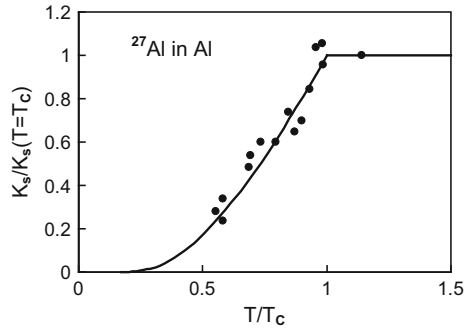
Equations (2.2.10) show that when τ_{so} is long there is only a small residual value of $\chi_{so}(T \ll T_c)$, but when it is short, i.e. strong spin-orbit scattering near surfaces, $\chi_{so}(T \ll T_c)$ is only slightly perturbed from its normal state value. The latter case is often found for heavy metals such as Hg [48] and Pb [45], and was also found for β Sn [46, 59]. These authors performed various doping experiments, which were also consistent with (2.2.10). Ferrell obtained a result similar to (2.2.10b) by means of a physical argument [51].

In a metal as light as elemental *Al* one might expect spin-orbit effects to be very small. Since colloids of *Al* are difficult to prepare, shift studies were performed on thin film samples. The first results gave, surprisingly, residual shift values of $\sim 75\%$ [47]. It appears that orientation of their multi-film samples was quite critical, as subsequent work [55] yielded a very small residual shift. Later measurements by Fine, et al., on a single thin-film sample [56] gave results in good agreement with the Yosida function [49]. These data are displayed in Fig. 2.6, finally giving verification to the BCS theory-based prediction.

T₁ Behavior Below T_c: The BCS Coherence Factor

The behavior of T_1 for an sp-band (Type I) superconductor according to the BCS theory was first investigated, theoretically and experimentally, by Hebel and Slichter [64]. We sketch the calculation of T_1 in the SC phase following the derivation in [9]. First, recall from Sect. 1.2.1 that the T_1 process consists of scattering fermions

Fig. 2.6 Data for the ^{27}Al Knight shift in Al metal from [56] are shown, plotted in units of the normal state shift as a function of T/T_c . The solid curve is the Yosida function, i.e. behavior expected on the BCS theory



from an initial state $|\mathbf{k}\sigma\rangle$ to a final state $|\mathbf{k}' - \sigma\rangle$, while the nuclear spin goes from m to $m \pm 1$ so that angular momentum is conserved. This outline is maintained in the SC state, but other circumstances change drastically. For $T < T_c$ there is some fraction of fermions which are paired ($|\mathbf{k}\sigma\rangle$ and $|\mathbf{k} - \sigma\rangle$) in the ground state and do not scatter. The quasiparticles not condensed into the ground state are thermally excited above the energy gap $\Delta(T)$ and are available to scatter as sketched above. The main differences are that, first, there appears in the summation in (2.2.5) a factor $C_{\pm}(\mathbf{k}, \mathbf{k}') = \frac{1}{2}[1 \pm (\Delta^2/E_{\mathbf{k}}E_{\mathbf{k}}')]$ known as the *coherence factor*, and second, the normal state density of states factors in the integrals leading to (2.2.7) are replaced by the BCS density of states $n_{BCS}(E) = n(E_F)E/(E^2 - \Delta^2)^{1/2}$, where $\Delta \leq E \leq \infty$. The coherence factor arises because of the pairing of electrons in the condensed phase, and is characteristic of many dynamic properties treated with BCS theory [19]. The choice of sign for $C_{\pm}(\mathbf{k}, \mathbf{k}')$ depends on whether the scattering perturbation is invariant under time reversal applied to the fermion bath. If it is, as in the case of phonons (e.g. ultrasonic attenuation) then $C_{-}(\mathbf{k}, \mathbf{k}')$ applies. If it is not invariant, such as for electromagnetic absorption and magnetic dipolar nuclear relaxation, then $C_{+}(\mathbf{k}, \mathbf{k}')$ applies.

For the superconducting nuclear relaxation rate $1/T_{1s}$ one finds, in units of the normal state rate $1/T_{1n}$,

$$\frac{T_{1n}}{T_{1s}} = \frac{2}{k_B T} \int_{\Delta}^{\infty} \frac{dE (EE' + \Delta^2) f(E) (1 - f(E'))}{[(E^2 - \Delta^2)(E'^2 - \Delta^2)]^{1/2}}, \quad (2.2.11)$$

where $E' = E \pm \hbar\gamma_n H$. Below T_c the excitation probability is the Fermi function $f(E_g) = [\exp(\beta E_g) + 1]^{-1}$ of the gapped energy $E_g = (E^2 + \Delta^2)^{1/2}$. Since the nuclear Zeeman energy $\hbar\gamma_n H$ is minuscule on the scale of the quasiparticle energy, there is in fact a logarithmic singularity in (2.2.11) for the case of the coherence factor $C_{+}(E, E')$. The most satisfactory explanation for how this singularity is “tamed” is by means of anisotropy of the gap energy $\Delta(T)$ [9, 65, 66]. The nuclear Zeeman energy will be neglected henceforward.

The behavior of T_{1n}/T_{1s} in (2.2.11) may be divided into two regions, $k_B T \ll \Delta(T)$ and $k_B T > \Delta(T)$. For $k_B T \ll \Delta(T)$ the integral is dominated by the peak in

$n_{BCS}(E)$ near the gap, which becomes very nearly constant $\Delta(T) \approx \Delta(0)$. In this limit the factor $f(E)(1 - f(E)) \approx \exp(-\beta\Delta(0))$, so that $1/T_{1s}$ decays exponentially at low T. In the other limit $k_B T > \Delta(T)$ (T near T_c), the factor $f(E)(1 - f(E))$ will have nearly its normal-state value, and the singularity in (2.2.11) has the potential to elevate T_{1n}/T_{1s} to values considerably in excess of 1. This is the source of the well-known BCS *coherence peak* in $1/T_1(T)$ at $T < T_c$. This peak was first measured on ^{27}Al in Al metal and identified by Hebel and Slichter [64], establishing a major milestone in experimental confirmation of the BCS theory.

It is important to note that for measurements such as ultrasonic attenuation the appropriate coherence factor to use is $C_-(\mathbf{k}, \mathbf{k}')$, whereupon the factor $(EE' + \Delta^2)$ in the numerator of (2.2.11) is replaced by $(EE' - \Delta^2)$. This effectively cancels the singularity at $E \simeq \Delta$. As a result, the ultrasonic attenuation coefficient was expected to fall abruptly below T_c , as had been confirmed experimentally [67]. This striking contrast between results obtained with probes having different symmetry properties was a very important confirmation of the correctness of the BCS picture.

Following the Hebel-Slichter results, Masuda and Redfield [65] reported further T_1 measurements on ^{27}Al in Al metal taken at temperatures ranging from above to well below T_c . Their results (Fig. 2.7) offered a full panorama of the BCS-theoretical behavior, with a coherence peak (in $1/T_1$) rising above the normal state Korringa curve by a factor ~ 2 , then descending into the superconducting state in a clearly exponential fashion. These data were obtained with a field-switching technique similar to that used in [64], the main difference being that pumped ^3He cooling allowed them to extend the measurements to 0.35 K, i.e. far below $T_c = 1.18$ K for Al metal.

Analyzing T_1 Data in the Superconducting State

Since the formulation of (2.2.11) has been widely employed to analyze SC-state data on high- T_c materials as well as all manner of unconventional superconductors, we recount here the analytic procedure used to fit the Al data in some detail [9, 65]. These results are referred to in other sections of the book as well.

In order to control the singularity in (2.2.11), Hebel and Slichter [64] postulated a broadening of the electronic energy levels. While such a device enabled them to obtain a reasonable result for the coherence peak, it lacked a clear physical basis. Masuda and Redfield, on the other hand, suggested that the observed peak was conditioned by a mild anisotropy of the gap parameter $\Delta(T)$. Not only does this give a better fit to the peak data, but it also has a clear physical origin in the BCS equations. There, the gap parameter is formally a function of \mathbf{k} , and the \mathbf{k} -independent gap parameter is just a convenient approximation used to solve the equations [66]. Ample theoretical evidence has been reported for gap anisotropy effects from van Hove singularities and other causes [68].

To illustrate the T_1 analysis with (2.2.11) we summarize briefly the development in [9] and [65], and refer the reader to these sources for a more detailed discussion. The procedure is to incorporate the gap anisotropy into the BCS density of states factors in (2.2.11) at the point where sums on \mathbf{k} and \mathbf{k}' are converted to energy integrals. We therefore back up a step from (2.2.11) and rewrite it as

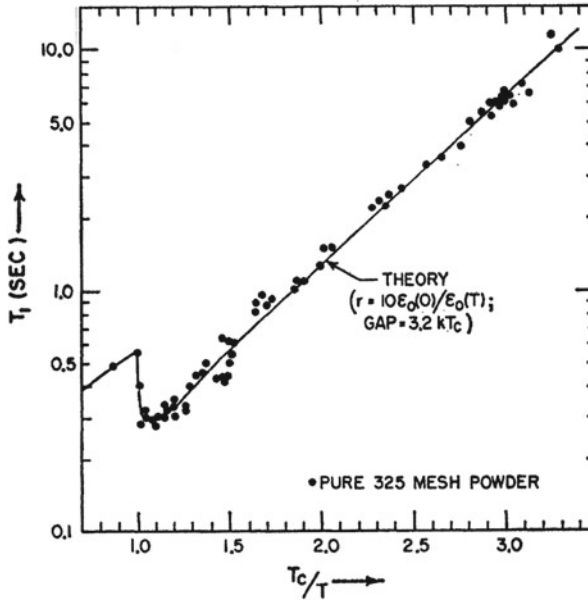


Fig. 2.7 A semilog plot of T_1 data for the superconducting state of Al metal versus T_c/T (dots) from [65]. Also shown is their fit of the data to the BCS theory (solid line), where the coherence peak (i.e. T_1 minimum) amplitude was adjusted using a distribution of energy gap values attributed to anisotropy. The low-temperature energy gap value is adjusted to the slope of the data, yielding $\Delta_0 = 3.2$ in reasonable accord with the BCS weak-coupling value of $3.52 k_B T_c$

$$\frac{T_{1n}}{T_{1s}} = \frac{2}{k_B T} \int_0^\infty [N_s(E)^2 + M_s(E)^2] f(E) (1 - f(E)) dE, \quad (2.2.12)$$

where

$$N_s(E) = \text{Re} \int_{a_1}^{a_2} \frac{E P(a) da}{[E^2 - \Delta(T)(1+a)^2]^{1/2}}, \quad (2.2.13a)$$

$$\text{and } M_s(E) = \text{Re} \int_{a_1}^{a_2} \frac{\Delta(T)(1+a) P(a) da}{[E^2 - \Delta^2(1+a)^2]^{1/2}}. \quad (2.2.13b)$$

In (2.2.13) the variation of Δ_k over the Fermi surface is represented as a distribution $P(a)$ extending over $a_1 \leq a \leq a_2$, where $\Delta_k \Rightarrow \Delta(T)(1+a)$ and $\int a P(a) da = 0$ by definition. As noted in [9], because the averaging over a is followed by integration over E , the precise shape of $P(a)$ is functionally immaterial to the final results. In fitting the T_1 data of Fig. 2.7, $\langle a^2 \rangle$ determines the depth of the T_1 minimum and $\Delta(0)$ fixes the slope of the exponential tail. The fit shown corresponds to $2\Delta(0) = (3.2 \pm 0.2) k_B T_c$ and $\langle a^2 \rangle^{1/2} \simeq 0.05$, in reasonable agreement with the BCS weak-coupling theoretical value $2\Delta(0) = 3.52 k_B T_c$. Comparable gap values are given by other probes [9].

There has also been extensive experimentation with doping effects on the SC T_1 behavior, yielding some interesting effects. For example, it was found that shortening the mean free path l of the quasi-particles led to even larger coherence peaks in the T_1 data for Al [69] and In-based [70] dilute alloys. This effect can be rationalized in terms of the theory of “dirty superconductors” [54], where potential scattering caused by impurities can become strong enough to cause effective mixing between Bloch functions on different parts of the Fermi surface. The result is a smoothing out of intrinsic gap anisotropy. Data for the Al-based systems was in good agreement with a theory of this effect [71], but for In-based alloys, there was only agreement for $l > \xi_0$, where ξ_0 is the coherence length. It was suggested that *gap inhomogeneity* might be suppressing the coherence peak in such a case. However, no further resolution of this point has apparently been reported.

As we shall see in the next subsection, there are a number of d-electron superconductors where T_1 has no coherence peak for reasons which are also not clear. Moreover, among high- T_c systems, suppression of the coherence peak in T_1 is universal, as is also the case for many *unconventional superconductors*. We defer further discussion of this point to subsections below, where fuller descriptions of the systems concerned are presented.

2.3 Static and Dynamic Magnetism in d-Band Metals

In this subsection we review the additional complexities which arise when a conductive solid has an open d-shell in addition to its sp-band effects. The d-electrons in solids are typically more tightly bound to their host ion, interacting more weakly with neighbors. As a result they have narrower, more highly structured energy bands with substantially higher densities of states at their Fermi surfaces. Moreover, they are subject to a *crystalline electric field* (CEF) which results from bonding and proximity to neighboring ions, which breaks the full rotational potential symmetry enjoyed by a free ion. As a result, the d-electron angular momentum “always” has a zero expectation value in the ground state. On the other hand, the greater densities of states of d-bands, when combined with the electron-electron exchange effects [57] which came quite clearly to light in the Moriya treatment of enhanced NMR shifts and relaxation [58], lead to strongly enhanced susceptibilities and even to permanently magnetized ground states in a number of pure metals (e.g. Fe, Co, and Ni in the 3d series). Moreover, ions with d-electrons as dilute impurities or dopants frequently possess a localized magnetic moment. As an example, the high- T_c materials do not exhibit localized magnetism *per se*, but the Mott insulators that they are derived from exhibit local-moment antiferromagnetism at low doping levels. When the d-holes become itinerant through doping, a localized d-electron spin Hamiltonian continues to be a reliable model for properties such as hyperfine (HF) effects, spin and Van Vleck paramagnetism, as well as hybridization effects with p-electron neighbors.

Special Features of NMR in d-Band Metals and Superconductors

Keeping superconductivity in mind, we shall restrict our attention to d-electron systems which do not order magnetically. We shall discuss, as an example, the behavior of the V_3X series of compounds, which are superconductors as well. There is a wealth of interesting NMR phenomena which arise in such systems, including:

- Prominence of the *core-polarization* (CP) d-spin HF field in studies of d-band magnetism. Since d-electrons have no contact interaction, this isotropic, negative HF coupling, which was identified by Heine [35] and by Wood and Pratt [35, 77], takes its place. The core polarization plays a major role, since dipolar interactions are often smaller and are cancelled by cubic symmetry.
- The greatly enhanced importance of orbital effects, both the static (Van Vleck) shift and susceptibility and the robust orbital T_1 mechanism. The d-band orbital susceptibility was first formulated by Kubo and Obata [36]. Its contribution to the NMR shift was identified by Clogston et al. [37] in connection with the V_3X compounds, where it had a profound effect on the interpretation of superconducting shift data.
- The latter authors [38] also pioneered the use of the $K - \chi$ plot as a means of analyzing NMR shifts and their corresponding susceptibility components in d-band metals. This technique continues to be used very widely and has led to great insight into the magnetic infrastructure of metals and intermetallic compounds. We present their method here.
- When d-electron metals are superconductive, they are nearly always Type-II superconductors. Thus, NMR studies are very often conducted in the *mixed state*, i.e. in the presence of a large magnetic field and a vortex lattice. The field penetrates throughout the sample, dividing itself into as many flux bundles as possible, which occurs when each vortex contains just one fluxon. We shall review results on NMR shifts, lineshapes, and on T_1 studies as well. These effects are directly relevant to superconductive high- T_c NMR studies, since they are largely conducted under the same conditions.

2.3.1 The d-Electron HF Interactions

In general there are two types of d-electron HF interactions, namely spin and orbital, the latter arising from the first term in (2.2.1), and the former from the second two terms. In d-band metals there are also multiple bands with their own Fermi surface density of states and corresponding HF interaction terms. These terms will make additional contributions to the NMR shift and relaxation rates, rendering the task of analyzing experimental data for these parameters a bit more complex. By and large, however, d-electron bands are somewhat more “lively” than their rather prosaic s and p counterparts, and tend to dominate the nuclear spin properties. In high- T_c materials, depending on your point of view, there is scant evidence for actual sp-bands *per se*, so the d-electron HF effects are, by any measure, the dominant ones.

Anisotropic d-Spin Susceptibility and HF Tensor

Allowing for anisotropic d-spin HF coupling, we then take

$$\mathcal{H}_{ds} = \sum_{\beta=x,y,z} A_{d\beta} I_{\beta} S_{\beta} \quad \text{with} \quad \chi_{d\beta} = \frac{N_A g_{\beta} \mu_B \langle S_{\beta} \rangle}{H}. \quad (2.3.1)$$

The d-spin shift coefficient is then defined as

$$\alpha_{d\beta} = \frac{K_{d\beta}}{\chi_{d\beta}} = \frac{A_{d\beta}}{N_A \gamma \hbar g_{\beta} \mu_B}. \quad (2.3.2)$$

For ordinary 3d metals we shall take $g_{\beta} \sim 2$, whereupon $\chi_{d\beta}$ becomes isotropic. However, these definitions carry over into the discussion of cuprates in Chap. 3, where there is evidence for substantial g-shifts. We also note here that the HF coefficient can be quoted as simply $A_{d\beta}$ in energy units, as $A_{d\beta}/\hbar$ in units of s^{-1} , as $A_{d\beta}/\gamma\hbar$ in kG/spin, or as $A_{d\beta}/\gamma\hbar g_{\beta}$ in units of kG/μ_B . Although it may be somewhat confusing, one finds all of these units in use in the high- T_c literature. The d-spin HF field is also known as the core-polarization HF field (hence $A_d \rightarrow A_{cp}$), which we now discuss.

Core-Polarization Hyperfine Coupling: The Mechanism

Since d-electron wavefunctions vanish at the site of the nucleus, they possess no direct contact HF field from the final term in (2.2.1). However, they do activate a contact HF term indirectly in such a way as to generate an effectively isotropic HF coupling term with the nuclear spins. This mechanism came to light with the work of Heine [35] and of Wood and Pratt [77]. Detailed calculations have been given by Freeman and Watson [72]. The mechanism of the *core polarization HF field* is a simple consequence of the Pauli exclusion principle, and works as follows. In d-electron atoms there are two or more filled s-shells which are magnetically inert. Nonetheless, these filled s-shells undergo repulsive coulomb interactions with the Fermi-surface d-electrons which, generally speaking, lie outside of them spatially. Thus, coulomb repulsion drives the s-shell electron orbitals closer to the nucleus. This repulsive effect is, however, dependent on spin. Consider the majority d-spin moment to point up. The up-moment s-shell electrons are then known to avoid close proximity with the up-moment d-electrons in a Pauli-exclusion effect known as the *Fermi hole*. The down-moment s-electrons have no such effect. With the same wavefunction, then, the down-moment s-electrons will have a higher coulomb repulsion energy. For that reason, a down-moment s-shell orbital will “shrink” toward smaller radii relative to the up-moment s-shell orbital, creating a *net down moment of s-electron density at the nucleus*, i.e. a net negative contact HF interaction. The differential orbital distortion effect is small, but the core s-shell HF couplings are enormous, so that there is a substantial net HF coupling from this effect. For 3d-electrons the resulting Hf field is $\sim -125 \text{ kG}/\mu_B$, increasing gradually across the 3d series. For the 4d and 5d shells the effect is generally larger [72]. As an example, we note that the $5\mu_B$ S-state moment of Mn^{2+} in MnF_2 generates a HF field $\simeq -127 \text{ kOe}/\mu_B$ at the ^{55}Mn nucleus. This compound has purely 3d-spin magnetism.

2.3.2 Orbital Shift and Susceptibility

The orbital term in (2.2.1) comes into play for both the NMR shift and T_1 . The orbital shift is driven by the Van Vleck orbital susceptibility, which was first formulated for band electrons in a simple model by Kubo and Obata [36]. The susceptibility was formulated in a tight-binding approximation, yielding the following expression for the β -axis susceptibility,

$$\chi_{orb} = N_A \Omega \mu_B^2 \int \frac{d\mathbf{k}}{(2\pi)^3} \sum_{nn'} \frac{f(E_{n\mathbf{k}}) - f(E_{n'\mathbf{k}})}{E_{n'\mathbf{k}} - E_{n\mathbf{k}}} \langle n\mathbf{k} | l_\beta | n'\mathbf{k} \rangle \langle n'\mathbf{k} | l_\beta | n\mathbf{k} \rangle, \quad (2.3.3)$$

where N_A is Avogadro's number, Ω is the atomic volume, and the summing indices n and n' represent the five d-orbital subbands as well as the spin quantum number. The quantity $f(E_{n\mathbf{k}}) = [\exp(\beta(E_{n\mathbf{k}} - E_F)) + 1]^{-1}$ is the Fermi occupation function. χ_{orb} is written here as a molar susceptibility.

Clogston et al. [76] have derived a companion expression to (2.3.3), which gives the induced orbital hyperfine field at the nucleus when the effects of the spin-orbit coupling and certain other terms in the general expression, deemed to be small, are neglected. The simplified expression is

$$H_{orb} = \Omega \mu_B^2 \int \frac{d\mathbf{k}}{(2\pi)^3} \sum_{nn'} \frac{f(E_{n\mathbf{k}}) - f(E_{n'\mathbf{k}})}{E_{n'\mathbf{k}} - E_{n\mathbf{k}}} \langle n\mathbf{k} | 2l_\beta / r^3 | n'\mathbf{k} \rangle \langle n'\mathbf{k} | H l_\beta | n\mathbf{k} \rangle, \quad (2.3.4)$$

where the field H is taken to be directed along the β axis. If we make the assumption that the radial functions of all the d-orbitals in the band are approximately the same, then we may extract $\langle 1/r^3 \rangle$ from the latter expression, finding

$$K_{orb} = [2\langle 1/r^3 \rangle / N_A] \chi_{orb}, \quad (2.3.5)$$

where the quantity in brackets is identified as the orbital shift coefficient α_{orb} . When using calculated ionic values for $\langle 1/r^3 \rangle$ [78], the foregoing authors suggest that a correction factor $\xi = \langle 1/r^3 \rangle_{metal} / \langle 1/r^3 \rangle_{ion} \simeq 0.75$ be invoked for realistic estimates of the metallic shift coefficient α_{orb} .

It should be noted that the foregoing expressions for the orbital shift and susceptibility were derived with the applied field assumed to be lying along a particular spatial axis. However, these calculations were originally presented in application to cubic d-band metals, for which no appreciable spatial anisotropy was expected to occur. In applications to high- T_c materials with their nearly 2D structures, these expressions are easily adapted to reflect the expected anisotropy. In such applications, we note that the orbital shift coefficient in (2.3.2) will be generally assumed to be isotropic.

Analysis of NMR Shift and Susceptibility for d-Band Metals: The (K, χ) Plot

With the foregoing additions to our list, we are now in a position to formulate a complete model of the shift and susceptibility of a d-band metal. The following

model would apply to a pure metal from the 3d, 4d, or 5d transition series, but also is intended to represent a binary or ternary intermetallic compound as long as its Fermi surface can be modeled with two bands, an sp-band which belongs mostly to the transition metal atoms and a d-band which belongs exclusively to the transition metal atoms. The p-orbitals on the ligands are assumed to be strongly mixed into the d-band, while the s-orbitals are not, i.e. are presumably nearly filled [38]. We then write for the susceptibility,

$$\chi_{tot} = \chi_{dia} + \chi_s + \chi_d(T) + \chi_{orb}, \quad (2.3.6)$$

where χ_s and $\chi_d(T)$ are the spin-paramagnetic terms, χ_{orb} is the d-electron orbital term given by (2.3.3), and χ_{dia} is the core diamagnetic term. Among these, χ_s is quite small, though its associated Knight shift may not be, so that any Landau diamagnetism is very small, indeed. Neither the latter nor χ_{dia} has any appreciable NMR shift effect [76]. Molar susceptibilities are used throughout this volume [79].

The NMR shift of the transition ion, then, has only three significant terms [76],

$$K(T) = K_s + K_d(T) + K_{orb} = \alpha_s \chi_s + \alpha_d \chi_d(T) + \alpha_{orb} \chi_{orb}, \quad (2.3.7)$$

in conventional notation for the shift coefficients. Typically, the only temperature dependence originates in $\chi_d(T)$. Therefore an experimental plot of $K(T)$ versus $\chi_{tot}(T)$ with T as the implicit variable should yield a straight line of slope α_d . An experimental K versus χ plot is just the beginning of a full (K, χ) analysis of the various terms in (2.3.6) and (2.3.7). Such an analysis for the case of Pt metal was presented in [76], with the plotted result shown here in Fig. 2.8. We give a brief account of the analytical procedure.

First, any $K - \chi$ analysis must begin at the origin, and several parameters need to be estimated in order to proceed. We refer the reader to the original paper for full details. The first step is to plot $\chi_{dia} \simeq -28 \times 10^{-6}$ emu/mol at $K = 0$ (point 1), since there is no appreciable diamagnetic shift [76]. This value of χ_{dia} is taken from the literature [80]. From point 1 we construct a line of slope α_s to extend over the interval $\Delta\chi = \chi_s$. For this step, α_s is obtained from HF structure parameters derived from optical data, yielding $\alpha_s \simeq 2.12 \times 10^3$ (emu/mol) $^{-1}$. χ_s is estimated using a free-electron model, where the number $n_{s,d}$ of (s, d) electrons satisfies $n_s + n_d = 10$. With a parabolic model for the 5d-band a value of $n_s = 10 - n_d = 0.2$ was obtained, giving $\chi_s \simeq 4.8 \times 10^{-6}$ (emu/mol). The s-band line in Fig. 2.8 then extends from point 1 to point 2. Next, we construct a line from point 2 with a slope equal to the estimated value of $\alpha_{orb} = 2\langle 1/r^3 \rangle / N_A$. The ionic value of $\langle 1/r^3 \rangle$ has been estimated to be 9.5 a.u. [79] from HF spectroscopic data, leading to the value $\alpha_{orb} \simeq 264$ (emu/mol) $^{-1}$, including a relativistic correction [76]. Drawing a line with slope α_{orb} from point 2, the intersection of that line with the line through the data (point 3) then partitions the remaining susceptibility into orbital and d-spin contributions as shown.

In the case of Pt metal, χ_{tot} is dominated by $\chi_d(T)$, and χ_{orb} is a relatively small fraction ($\simeq 15\%$) of χ_{tot} . In cases where χ_{orb} is a significant fraction of the total, its temperature dependence may be a big enough effect so that a simple (K, χ) plot

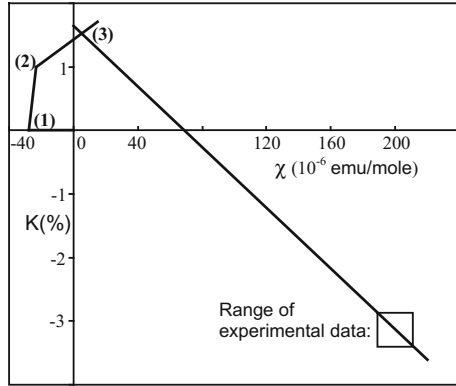


Fig. 2.8 A K - χ plot is shown for ^{195}Pt in Pt metal from [76]. Plotting successive contributions to (K, χ) carries one from the origin to point 1 (χ_{dia}), then from point 1 to point 2 (K_s, χ_s), and finally from point 2 with an estimated slope α_{orb} . The intersection at point 3 with the line through the experimental data completes the partition of the susceptibility. A detailed discussion of the analysis is given in the text

is no longer reliable [76]. Nonetheless, the (K, χ) method has been widely used to analyze NMR shift data with experimental susceptibilities. For example, it was used to determine that substantial χ_{orb} terms were present in the V_3X 's and in V metal [37]. We reproduce in Table 2.3 the table of results from [37].

In this table, values of χ_{orb} from (K, χ) analyses are subtracted from experimental susceptibilities to estimate χ_d , which is given as $\chi_{expt} - \chi_{orb}$. The latter values are then to be compared with d-spin susceptibilities estimated from the specific heat coefficient γ , where $\chi_{sp.ht.} \simeq 3\mu_B^2\gamma/\pi^2k_B^2$. A simple theory gives electron-phonon enhancement of γ by a factor $[1 + N(0)\mathcal{V}]$. \mathcal{V} is the BCS electron-phonon interaction parameter. Since χ_d is not so enhanced [84], one may estimate $\mathcal{V}N(0) \simeq \chi_{sp.ht.}/\chi_d - 1$. In the last two columns of Table 2.3, values of $N(0)\mathcal{V}$ deduced in that way are compared with those derived from T_c using the BCS formula $N(0)\mathcal{V} = [\ln(0.855\theta_D/T_c)]^{-1}$. Considering the difficulty of estimating the relevant

Table 2.3 Table of susceptibility components and BCS parameters for V_3X compounds and V metal. The estimates for χ_{orb} were determined using (K, χ) plot analyses. The values of $\chi_d \simeq \chi_{expt} - \chi_{orb}$ so deduced are checked using density-of-states estimates from specific heat data as corrected for electron-phonon enhancement by means of BCS theory. See text for detailed explanation. All susceptibilities are in units of 10^{-4} emu/mol

	$R \equiv \chi_d(0)/\chi_d(T_c)$	χ_{expt}	χ_{orb}	$\chi_{sp.ht.}$	$\chi_{expt} - \chi_{orb}$	$N(0)\mathcal{V}$ (<i>Sp.Ht.</i>)	$N(0)\mathcal{V}$ (BCS)
V_3Ga	$0 \leq R \leq 0.25$	17.9	5.2–7.5	14.0	12.7–10.4	0.13–0.39	0.35
V_3Si	$0 \leq R \leq 0.25$	15.7	5.2–7.5	10.7	10.5–8.2	0.09–0.35	0.35
V		3.08	2.11	1.22	0.971		0.244

parameters, this analysis gives a nicely consistent picture in which it is established that (a) χ_d at $T \ll T_c$ is a small fraction of its normal-state value, and (b), values of χ_d consistent with electron-phonon enhancement of γ are obtained. Note that $\chi_s \simeq 0.3$ (units of Table 2.3) has been ignored and is essentially negligible.

2.3.3 Spin-Lattice Relaxation Effects for d-Band Electrons

An open d-band brings added richness—and complications—to the T_1 process as well, contributing a total of three additional terms to the T_1 rate. These are the d-spin core polarization (CP), the d-spin dipolar, and the d-orbital terms. The d-orbital relaxation process was first discussed by Obata [81]; we shall spell out the results of that calculation below. The general treatment of the CP relaxation process, on the other hand, is an enterprise of great complexity. Under a set of straightforward restrictions, Yafet and Jaccarino have presented a very clear discussion of this problem [82], which has been useful under a variety of circumstances. Here we discuss briefly the approximations employed and give the results.

The stated approximations are as follows:

- Spin-orbit coupling is disregarded.
- The unperturbed states (i.e. without HF terms) are taken to be Hartree-Fock solutions of the simplified Hamiltonian.
- Exchange integrals responsible for the CP effect are treated in first order.
- Exchange effects between conduction band orbitals are neglected.
- Conduction band states are self-consistent Bloch states, which are admixtures of s, p, and d orbitals.
- The conduction band d-states are treated in a tight-binding approximation.
- Finally, consideration is limited to the case of a cubic metal. As a result, the cross terms between sp and d-orbital matrix elements can be shown to vanish.

The resulting expressions for the shift and relaxation rate are:

$$K = \frac{4\pi}{3} (\gamma_e \hbar)^2 [\langle \phi_s^2(0) \rangle (1 - F_d) - |\phi_{cp}(0)|^2 F_d] n(E_F) \quad (2.3.8)$$

and

$$\frac{1}{T_1 T} = \frac{4\pi k_B}{\hbar} \left[\frac{4\pi}{3} \gamma_n \gamma_e \hbar^2 \right]^2 \left[\langle \phi_s^2(0) \rangle (1 - F_d)^2 + |\phi_{cp}(0)|^4 F_d^2 \left(\frac{1}{3} f^2 + \frac{1}{2} (1 - f)^2 \right) \right] n(E_F)^2, \quad (2.3.9)$$

where F_d is the fraction of d-character of all the states at the Fermi surface, and $n(E_F)$ is the total density of states (of all “bands”) at the Fermi surface. Thus, even if there is appreciable s-d mixing in the Bloch functions the contributions to shift and relaxation will occur separately as shown. CP terms are only kept for the d-orbitals, even though they may occur in the calculation for the s and p orbitals. The reason

for this is that the contact terms dominate the sp regions of the Fermi surface, and any CP terms are neglected for those states as small corrections.

The parameter f gives the relative weight of Γ_5 character for d-orbitals at the Fermi surface, while $1 - f$ gives the proportion of Γ_3 character [83]. It is seen that the sp-contact and d-CP portions of the formulas for K and $1/T_1T$ obey separate Korringa-like relations (see (2.2.8)), where the Korringa relation for the CP terms has a reduction factor $q(f) = \frac{1}{3}f^2 + \frac{1}{2}(1 - f)^2$, i.e.

$$\frac{1}{T_{1cp}T} = \frac{4\pi k_B}{\hbar} \left[\frac{4\pi}{3} \gamma_n \gamma_e \hbar^2 |\phi_{cp}(0)|^2 \right]^2 n_d(E_F)^2 q(f) = \frac{4\pi k_B \gamma_n^2}{\hbar \gamma_e^2} K_{cp}^2 q(f), \quad (2.3.10)$$

where the second equality shows the modified Korringa relation. $q(f)$ is essentially a degeneracy factor, having a value 1/2 for the two Γ_5 orbitals ($f = 1$), 1/3 for the three Γ_3 orbitals ($f = 0$), and 1/5 when all five d-orbitals are equally weighted ($f = 0.6$). Thus the five d-orbitals contribute independently to $1/T_{1cp}$, very much like the fluctuations of separate magnetically-active neighbors contribute to the T_1 process of a ligand nucleus [62]. The difficulty in utilizing (2.3.10) is that the parameter f for d-band metals is generally unknown.

The orbital T_1 process was first discussed in detail by Obata [81], treating both orbital and dipolar relaxation rates in the same calculation. As with the CP calculation above, spin-orbit coupling is neglected, the d-orbitals are treated in a tight-binding approximation, and the system considered is a cubic metal. There are no cross terms between orbital and spin-scattering relaxation processes. It was noted in [82] that the dipolar process has interference with the contact and CP processes, but if the states at the Fermi surface can be separated into a d-band and an sp-band, then the interference terms vanish. For a cubic metal, both the orbital and dipolar relaxation rates are isotropic, but both depend on the symmetry parameter f , according to

$$\frac{1}{T_{1orb}T}, \left[\frac{1}{T_{1dip}T} \right] = \frac{4\pi k_B}{\hbar} [\gamma_n \hbar H_{orb}]^2 n_d(E_F)^2 p(f), [d(f)], \quad (2.3.11)$$

where $H_{orb} = 2\mu_B \langle 1/r^3 \rangle$, $p(f) = \frac{2}{3}f[2 - \frac{5}{3}f]$, and $d(f) = \frac{5}{49}[\frac{1}{3}f^2 + \frac{2}{5}(1 - f)]$.

Comparison of the dependences of $q(f)$, $p(f)$ and $d(f)$ on f is shown in Fig. 2.9. The orbital relaxation rate ($p(f)$) is seen to vary from zero, when the Γ_5 orbitals alone are occupied at the Fermi surface, to a maximum when all five orbitals are equally occupied, since the orbital matrix elements between the two symmetries are the largest ones. The dipolar relaxation rate ($d(f)$) varies only slightly across the full range of f , but it is only about 10% of the average value of $p(f)$. Thus, the dipolar relaxation is only significant when $p(f)$ is near zero.

The complete list of magnetic relaxation processes for d-band metals is then

$$1/T_1 = 1/T_{1s} + 1/T_{1cp} + 1/T_{1orb} + 1/T_{1dip}. \quad (2.3.12)$$

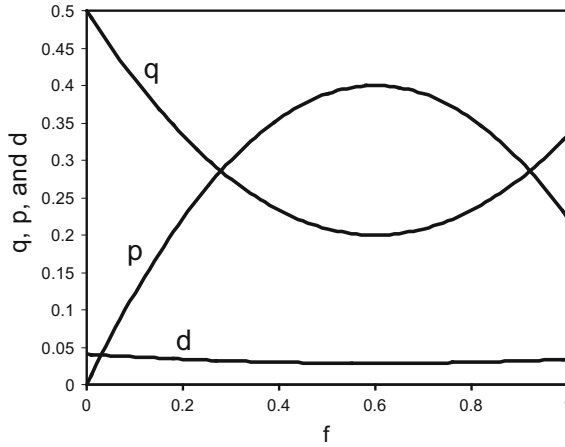


Fig. 2.9 The symmetry factors $q(f)$, $p(f)$, and $d(f)$ pertaining to CP, orbital, and dipolar relaxation rates discussed in the text, respectively, are plotted as a function of the fraction f of Γ_5 character in the relevant d-band orbitals at the Fermi surface. The point $f = 0.6$ represents equal weight of all five d-orbitals and is the maximum and minimum point of $p(f)$ and $q(f)$, respectively. In many cases the dipolar rate is negligible, as it is only $\sim 9\%$ of the average value of the closely related orbital rate

We illustrate the analysis of experimental T_1 rates into these different contributions with calculations given by [82] for d-band metals V and Nb. In stating these results we define $H_s = (8/3)\pi\mu_B\langle\phi_s^2(0)\rangle$ and $H_{cp} = (8/3)\pi\mu_B|\phi_{cp}(0)|^2$, whereupon (2.3.9) becomes

$$\frac{1}{T_{1s,cp}T} = \frac{4\pi k_B}{\hbar} [\gamma_n \hbar H_{s,cp}]^2 n_{s,d}^2 [1, q(f)] \quad (2.3.13)$$

for the s-band and CP contributions. The parameters $H_{s,cp}$ are the HF fields per unit of spin from these sources. The T_1 contributions from the three main sources have been estimated [82] for V and Nb metals as listed in Table 2.4. For this purpose, H_s has been estimated using data from the literature [82], and H_{cp} and H_{orb} have

Table 2.4 Table of HF parameters and specific heat densities of states leading to estimates of $(T_1 T)^{-1}$ for elemental V and Nb using the formulas given in the text. The total relaxation rates are stated for $f = 0.6$, but would not change significantly for other values of f . The theoretical estimate undoubtedly exceeds the experimental numbers because of the electron-phonon enhancement of the specific heat density of states, which does not affect nuclear relaxation rates. See text for data sources and additional discussion. HF fields are given in units of 10^6 Oe, densities of states in states/eV-atom, and relaxation figures in $(sK)^{-1}$

	H_s	H_{cp}	H_{orb}	$n_s(E_F)$	$n_d(E_F)$	R_s	R_{cp}	R_{1orb}	$(T_{1calc}kT)^{-1}$	$(T_{1exp}T)^{-1}$
V	1.12	-0.117	0.19	0.12	1.84	0.642	1.65	4.35	2.86	1.27
Nb	2.48	-0.21	0.285	0.14	1.66	3.76	3.74	6.9	7.55	2.8

been derived from Hartree-Fock calculations given by Freeman and Watson [78]. The total densities of states for these elements are taken from specific heat measurements, where the s-band components are estimated assuming for simplicity one s-electron per atom. The quantities R_s , R_{cp} , R_{orb} are defined to be the expressions given above for $1/T_1 T$ from these sources *without the symmetry factors* [$1, q(f), p(f)$]. The experimental values of $(T_{1exp} T)^{-1}$ are data reported by Butterworth [85].

What this table shows is that the CP and orbital mechanisms of relaxation are important. For the lighter metals, where the s-band contribution is smaller, these d-electron terms may even be the dominant ones. On the other hand, we see that the specific heat density of states clearly overestimates the relaxation rates, pointing to a substantial electron-phonon enhancement effect for V and Nb metals (which are also superconductors). In [9] a quantitative discussion of the latter effect is given, finding reasonable agreement between the nuclear relaxation data and estimates from other measurements, somewhat like the comparisons in Table 2.3. As the details go beyond the intended scope of this discussion, the reader is referred to [9] and references therein for further discussion.

This completes our discussion of normal-state NMR shift and relaxation effects in transition metals. The mechanisms in (2.3.7) and (2.3.12) are the foundation of effects to be found in high- T_c materials, though the details remain to be worked out. We next consider the effects of Type II superconductivity in the d-band metals.

2.3.4 NMR Studies of 3d Metals as Type-II Superconductors

The type-II superconductivity of d-band metals and intermetallic compounds presents a rather different set of problems from those of the type-I systems discussed in Sect. 2.2.2. First, type-II systems exhibit great complexity of behavior in a magnetic field, showing three phases as a function of the magnitude of the applied field for $T < T_c$ and exhibiting two critical fields, H_{c1} and H_{c2} . Below H_{c1} there is the typical Meissner exclusion of all magnetic flux except for the usual penetration depth λ .

Between H_{c1} and H_{c2} there is a state of essentially complete, but inhomogeneous field penetration in the form of superconducting current vortices which allow a single fluxon of field to exist in a region of normal (i.e. nonsuperconducting) metal with a diameter $\sim \xi_0$, the Pippard coherence length. Of course, the magnetic field of a fluxon penetrates the surrounding material to a depth of $\sim \lambda$. Each fluxon comprises one flux quantum $\Phi_0 = hc/2e = 2.07 \times 10^{-7} \text{ G cm}^2$.

Because of the accommodation of type-II superconductivity to applied fields through the penetration of vortices, the superconducting state can persist up to fields much higher than the thermodynamic critical field H_c .⁹ One can make a rough estimate of H_{c2} using a picture of vortices with normal cores of approximate radius ξ_0 . In the mixed state with field H ($T \ll T_c$) the density of vortices is H/Φ_0 . The fraction

⁹ H_c is defined as the field giving the field energy density $H^2/8\pi$ equal to the condensation energy into the superconducting state [18].

of normal sample material is then $\sim \pi \xi_0^2 H / \Phi_0$. Setting this expression equal to 1 gives an estimate $H_{c2} \sim \Phi_0 / \pi \xi_0^2$. This is only slightly larger than the expression deduced from Ginzburg-Landau (GL) theory,

$$H_{c2} = \frac{\Phi_0}{2\pi \xi_0^2}. \quad (2.3.14)$$

As was first demonstrated by Abrikosov [92], the normal-superconducting boundary wall has positive energy for $\lambda < \sqrt{2}\xi$. However, if the GL parameter $\kappa = \lambda/\xi > \sqrt{2}$, then the boundary wall has negative energy, so that the system will lower its free energy by making the boundary area as large as possible. Thus, the field arranges itself into individual fluxons, each surrounded by a normal-superconducting wall. In this way we see that the condition $\kappa > \sqrt{2}$ is the *definition of a type II superconductor*, κ being the GL parameter. Abrikosov predicted the existence of such a *mixed state*, in which the vortices arrange themselves (in reasonably clean material) into an ordered lattice if $\kappa = \lambda/\xi > \sqrt{2}$ [92]. The lowest energy state of such a lattice was shown to be minimized by a triangular arrangement of vortices by Kleiner et al. [93]. Below, we describe NMR spectra which are consistent with this theoretical conclusion.

It is interesting to look at simple expressions for ξ and λ to see why there is a general tendency for d-electron superconductors to exhibit type-II superconductivity. The expressions

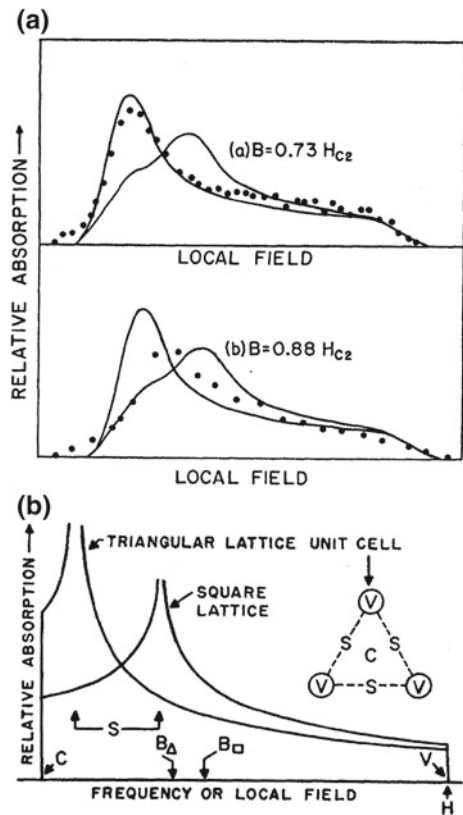
$$\lambda_0 = \left[\frac{m c^2}{4\pi n_s e^2} \right] \quad \text{and} \quad \xi_0 = a \frac{\hbar v_F}{k_B T_c}, \quad (2.3.15)$$

where a is a constant of order unity, come from the London equations and from Pippard's uncertainty principle argument, respectively. Since d-bands tend to have large effective masses and high- T_c materials in particular have low carrier densities n_s , we expect λ_0 values to be larger than for sp-band superconductors. Furthermore, small values of E_F (and thus of v_F) as well as higher values of T_c will make for short ξ_0 's. Thus, it is generally expected that $\lambda > \sqrt{2}\xi_0$. As an example, we mention V_3Si , a superconductor at ~ 17 K which we shall discuss further below. Here, we only note that Greytak and Wernick [94] reported a measurement of $\lambda_0 = 1500$ Å and a related estimate of $\xi_0 = 25$ Å. Thus, $\kappa \simeq 60$ and from (2.3.14) we estimate $H_{c2} \simeq 530$ kG. A second estimate can be made from the thermodynamic critical field $H_c = 6370$ G [86] and the measured value of λ_0 using (4–62) from [18], $H_{c2} = 4\pi \lambda_0^2 / \Phi_0$. This yields $H_{c2} = 550$ kG which is in surprisingly good accord with the previous number. In any case, V_3Si is a very “hard” superconductor, indeed.

Internal Field Distributions in the Mixed State from NMR Studies

NMR studies of type-II superconductors are typically done in the mixed state, i.e. for $H_{c1} < H < H_{c2}$. There is substantial NMR line broadening from spatially-dependent shielding supercurrents in the mixed state. We shall first review studies conducted to map the distribution of such currents, after which we will look at shift and relaxation studies. A number of internal field studies have been reported for V and Nb metals

Fig. 2.10 **a** Distributions of diamagnetic shielding fields measured using *rf* saturation of the ^{51}V NMR in superconducting V metal, and **b** simulations of internal field distributions under similar circumstances for both square and triangular vortex lattices. In **(a)** results are given for $T \simeq 1.4\text{ K}$ and for fields of $0.73 H_{c2}$ and $0.88 H_{c2}$ as shown, where $H_{c2} = 2720\text{ G}$. For **(b)** the field simulations were done on the basis of solutions of the Ginzburg-Landau equations in the Abrikosov limit. The inset shows the triangular lattice unit cell, with points there and on the distribution labelled V, S, and C corresponding to a vortex (V), a saddle point (S) showing a divergence, and the minimum field (C)



[87–89]. We review briefly the results given by Redfield [87], who conducted the following field-switching NMR experiment on ^{51}V in V metal. The sample was polarized in $\simeq 10\text{ kG}$, after which the field was switched to a value below $H_{c2} \sim 3,000\text{ G}$ for a time of 0.1 s , during which an *rf* field was applied transverse to the steady field. The field was then switched back to 10 kG where the nuclear polarization was recorded. By scanning the frequency of the *rf*, the spectrum of internal fields was able to be mapped out. Results from this study are shown in Fig. 2.10a for two field values. These data have been fitted to calculated internal field distributions based on the GL equations in the Abrikosov limit, assuming both square and triangular lattices. The raw calculated distributions are shown in Fig. 2.10b. Fits are carried out by convoluting the latter distributions with a Gaussian of adjustable width, then adjusting the width and total area for best fit.

The triangular lattice unit cell is shown as an inset to Fig. 2.10(b), where the points V, C, and S are seen to correspond to the maximum field, minimum field, and the singularity in the distribution, respectively. The singularity appears much closer to C for triangular lattice than for the square lattice. Results for the lower field value ($\simeq 0.73 H_{c2}$) are seen to be in good accord with the triangular lattice. The higher

field value is rather closer to H_{c2} , where a kind of gapless superconducting state sets in and there are many corrections to the simple field-distribution calculation. Thus, it is not surprising that the simple triangular lattice calculation is no longer accurate [87]. Studies of effects near H_{c2} are reviewed in [9]. We shall, however, restrict our attention here to the region $H_{c1} \ll H \ll H_{c2}$.

It is interesting to compare the field distribution results from [87] with theoretical predictions. For example, the results from Kleiner, et al. [93] predict that $H_V - H_S = 1.35 (H - B)$. From [87] we find for the conditions of Fig. 2.10 the experimental value $H_V - H_S = 285 \text{ G}$, while under the same conditions $1.35 (H - B) \simeq 165 \text{ G}$, a considerable underestimate. On the other hand, according to the Abrikosov solution [9, 92] $1.35 (H - B) = 1.35 (H_{c2} - H)/\beta_a(2\kappa^2 - 1)$, which we find to be 520 G , which is a considerable overestimate. For this purpose we take $\beta_a = 1.16$ for the triangular lattice from [93] and obtain $\xi_0 = [\Phi_0/2\pi H_{c2}]^{1/2} = 348 \text{ \AA}$. The estimate $\lambda = 400 \text{ \AA}$ [91] then gives $\kappa = 1.15$. Substantial corrections to these simple theoretical results have been given by Eilenberger [90].

The NMR Shift in Type-II Superconductors

In the foregoing study of elemental vanadium, the precision with which the vortex lattice could be characterized was not great enough to resolve changes in the d-spin shift $K_d(T)$ below T_c [87]. However, in a truly *hard* type-II system where $\kappa \gg 1$, it is possible to resolve small shift changes at field values such that $H_{c1} \ll H \ll H_{c2}$. The reason for this is that the NMR lineshape is then strongly dominated by the singularity from the saddle regions S (Fig. 2.10b), which is therefore shifted only slightly away from the applied field. Moreover, the NMR linewidth from diamagnetic shielding is typically only modestly greater than one might find in the normal state.

We illustrate these points with data and discussion of the closely related cases of V_3Si and V_3Ga , where V_3Si was touted earlier as a truly hard superconductor.

Interestingly, somewhat before the nature of the type-II diamagnetic shielding was investigated in detail in the 1960s, The NMR shifts in these compounds of both ^{51}V and ^{71}Ga were reported by Clogston et al. [37]. We reproduce their (K, χ) plot in Fig. 2.11. The interesting point here is that all NMR shift values here are consistent with the interpretation that, at $T = 1.8 \text{ K}$, the corresponding d-band susceptibility is diminished to $\sim 25\%$ of its value at 20 K . Further, its low temperature value is smaller than that at room temperature. Since these NMR shifts were measured in the mixed state at a field of 14 kOe , where they found “negligible diamagnetic *rf* susceptibility” [37], one can only conclude that spurious frequency shift effects from the diamagnetic shielding are negligibly small in comparison. Note that the total range of ^{51}V shift values here is only $\sim 0.1\%$.

It is interesting to consider the nature of the internal field distribution in V_3Si given the values of its parameters ξ_0 and λ_0 (25 \AA and 1500 \AA , respectively) stated above. First, the second moment of this distribution has been calculated by Pincus et al. [86], yielding the expression

$$\langle \Delta H^2 \rangle_{av}^{1/2} \simeq \frac{\Phi_0}{4\pi^{3/2}\lambda^2} \quad (2.3.16)$$

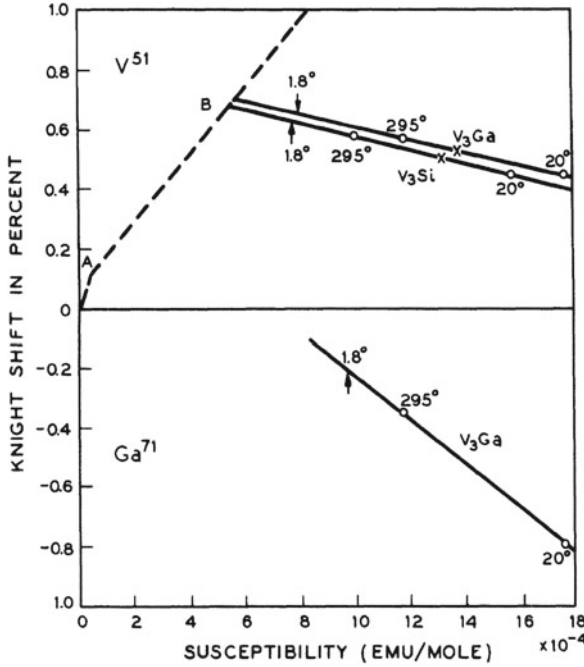


Fig. 2.11 Measured Knight shifts are plotted versus molar susceptibilities for ^{51}V in both V_3Si and V_3Ga and for ^{71}Ga in V_3Ga [37]. For the ^{51}V shifts a (K, χ) construction is shown, including the s-band contribution (point A) and the orbital contribution (points A–B), which intersects with lines through the data points. For the ^{71}Ga the results clearly show a transferred shift which is driven by the temperature-dependent d-band susceptibility. In both cases the location of the shift values measured at 1.8 K are shown, indicating that the negative CP shift is diminished to $\sim 75\%$ of its value at 20 K, and that the values of $|K_d(T)|$ in both cases are smaller than the values found at room temperature

under conditions where not only $H_{c1} \ll H \ll H_{c2}$ holds, but also $\lambda/d \gg 1$, where d is the separation of vortices in the mixed state. At $H = 14\text{ kOe}$ (i.e. for the data of Fig. 2.11), we find $d = [2\Phi_0/\sqrt{3H}]^{1/2} = 413 \text{ \AA}$ for the triangular lattice, giving $\lambda/d = 3.6$. For these conditions (2.3.16) gives $(\Delta H^2)_{av}^{1/2} = 41 \text{ Oe}$ for a square lattice. This may be a slight overestimate, but is of the right order, since the measured peak-to-peak derivative linewidth is $39 \pm 5 \text{ Oe}$ [86]. It is interesting to note in this case, where $\kappa \gg 1$, the Abrikosov relation ([92]) yields $H_V - H_S = 86 \text{ G}$, barely twice the second moment estimate.

We therefore find for the hard type-II superconductors that it is quite feasible to measure shift values with weak temperature dependences in the mixed state of superconductivity. This is a very important result for high- T_c NMR studies.

2.3.5 T_1 Phenomenology for Type-II Superconductors

In this final subsection of Chap. 2 we review T_1 behavior at $T < T_c$ for type-II d-band superconductors. Because of the complications which attend the measurement and interpretation of T_1 in the *mixed state* of these systems, our discussion of this topic will be limited to a few simple cases. A clear and thorough discussion of these effects, in terms of both theory and experiment, is given in [9]. The hallmarks of type-I system T_1 behavior are the coherence peak (in T_1^{-1}) just below T_c and the exponential decay $T_1^{-1} \propto \exp(-\Delta_0/k_B T)$ for $T \ll T_c$. For type-II systems these behaviors carry over in a modified way or not at all. The differences found between type-I and type-II behavior appear to be caused by the field penetration in the mixed state and the consequent spatial inhomogeneities.

The Coherence Peak Region, $T \leq T_c(H)$

Caroli et al. have shown that in the vicinity of a vortex core the excited state energies are diminished to $\Delta E \sim \Delta_0^2/E_F \ll \Delta_0$ [107]. Thus, for points near the (H, T) phase boundary, i.e. for H near $H_{c2}(T)$, there is a gapless region which has received a detailed theoretical examination [95–97]. The fluctuation (i.e. T_1) properties in this region are different from a type-I system and appear to depend on whether the carriers have a long mean-free path $l \gg \xi_0$ (“clean”) or whether it is short $l < \xi_0$ (“dirty”). In the simpler dirty limit case the electronic properties are local in character, and Cyrot [98] has derived the relation

$$\frac{T_{1n}}{T_{1s}} = 1 + \frac{ec}{\sigma k_B T_c} (H_{c2} - H) g(t), \quad (2.3.17)$$

where $t = T/T_c$, σ is the normal state conductivity and $H_{c2} = H_{c2}(T)$. This relation is only valid for $(H_{c2} - H) \ll H_{c2}$, so that it only gives the slope $T_{1n} d(T_{1s}^{-1})/dH$ near H_{c2} . The function $g(t) > 0$ for $t > 0.6$, while $g(t) < 0$ below that point. One must be very careful in using (2.3.17) to interpret actual data, since T_1 is usually measured by scanning temperature rather than field.

Masuda and Okubo have obtained T_1 data on ^{51}V in V_3Sn , a superconductor with $T_c \simeq 3.6\text{ K}$ (their sample) and $H_{c2}(0) = 16\text{ kG}$ [99, 100]. Their data are shown for three values of applied field in Fig. 2.12. These authors used (2.3.17) to show that

$$d(T_{1n}/T_{1s})/dT \propto g(t) \quad (T \leq T_c(H)), \quad (2.3.18)$$

as well, and have evaluated the constant of proportionality. We note that for $H = (4470, 8940, 13410)\text{ G}$, $T_c(H) = (3.2, 2.6, 1.8)\text{ K}$ and thus $t(H_{c2}) = (0.89, 0.72, 0.50)$ for the three data curves in Fig. 2.12. Thus, the slopes of the data plots at $T \leq T_c$ are nicely consistent with these parameters, since $d(T_{1n}/T_{1s})/dT$ is positive for the first two, then turns negative for the third, where $t(H_{c2})$ falls below 0.6. It seems, then, that measurements at low (or zero) field on V_3Sn yield a conventional BCS coherence peak, but that it is gradually quenched out by fluxoids at higher field values.

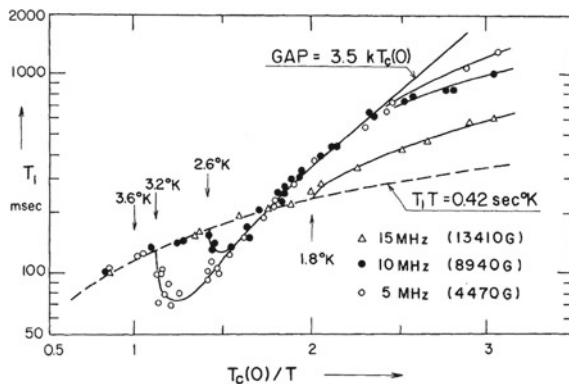


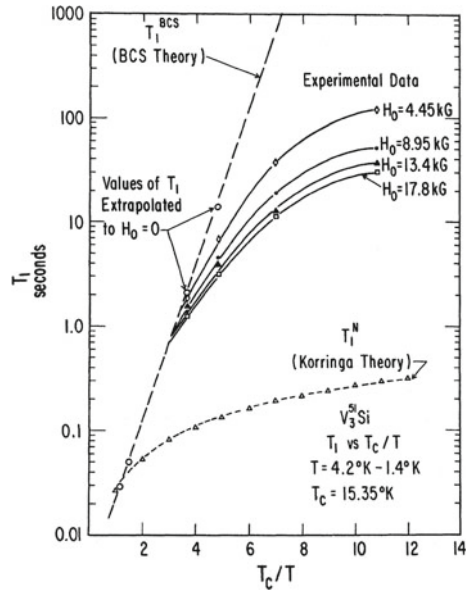
Fig. 2.12 A semilog plot of data for T_1 of ^{51}V in V_3Sn versus $T_c(0)/T$ in the superconducting state for three values of applied field as shown from [99]. The data shown exhibit coherence peaks for 1341 and 8940 G, but not for 13410 G. All three plots show deviations from the exponential BCS behavior at the lowest temperatures, an effect attributable to spin diffusion to the normal cores. See text for discussion

We mention three other cases of type-II T_1 studies at $T \leq T_c$. Each is somewhat anomalous in its own way. The first is the case of elemental V metal [101], where no convincing coherence peak was observed. The authors considered a number of possible explanations, finally suggesting that the T_1 peak may be suppressed by trapped flux. However, sometime after these results were published, the theory of T_1 in the clean limit emerged [95], and this interpretation was applied to the case of vanadium by Pesch [97]. The result was a good fit to the data for both samples [101], with no sign of a coherence peak. It seems, then, that coherence peaks will appear at low fields in the dirty limit, but not in clean samples.

No coherence peaks were observed in any of the V_3X compounds, where $\text{X} = \text{Ga}$, Si , Ge , and Pt , in the study conducted by Silbernagel et al. [102, 103]. The ostensible reason for this is disorder caused by the “Martensitic” structural transformation which was reported at temperatures just above T_c in these compounds [104, 105]. The authors offer no further discussion of the point [103].

The most anomalous case to be reported was that of niobium [106]. The relaxation of ^{93}Nb nuclear spins was studied in the SC state at field values varying from 2.40 kG up to 6.80 kG corresponding to T_c values which vary from 6.8 K down to 3.0 K. Using (2.3.14), H_{c2} corresponds to $\xi_0 \sim 200 \text{ \AA}$, so that the given mean-free path $l \simeq 140 \text{ \AA}$ is on the borderline between the clean and dirty cases. In any case, the T_1 data were found to fit the gapless theory [96, 97] for the higher field values. For the lower two field values, however, the T_1 data were found to execute a deep minimum just below $T_c(H)$, contrary to the gapless theoretical fits. Such behavior is clearly reminiscent of the V_3Sn data in Fig. 2.12, and one might inquire as to whether the calculation of $d(T_{1n}/T_{1s})/dT$ given in [100] based on (2.3.17) could be applied in this case. The authors did such a calculation and found that the coefficient of $g(t)$ for Nb is smaller

Fig. 2.13 A semilog plot of data for T_1 of ^{51}V in V_3Si versus T_c/T in the superconducting state for four values of applied field as shown from [102]. The data shown exhibit no coherence peaks, but follow exponential BCS theory behavior up to $T_c/T \sim 4$. Beyond that point the mechanism of spin diffusion takes over, giving a relaxation rate which is proportional to the applied field (i.e., to the fluxoid density), as expected. See text for further discussion



by a factor 150–200, so that similar behavior cannot be expected on that basis. There seems to be no straightforward explanation for this anomalous result.

Type-II T_1 Behavior for $T \ll T_c$

For values of T well below T_c , an exponential decay $T_{1s}^{-1} \propto \exp(-\Delta_0/k_B T)$ has generally been found to appear. However, as this intrinsic BCS rate weakens, another contribution attributable to the fluxoids is often seen. Since the energy gap near the fluxoids is very small [107], T_{1s} for a region of area $\sim \xi_0^2$ is essentially that of the normal state. When the BCS T_1 process in the bulk of the SC material becomes very slow, then a process whereby the nuclear polarization diffuses to the normal cores becomes predominant. This process was found to be present in three of the four examples given above [99, 101, 102] but was studied most systematically in the case of V_3Si [102].

^{51}V T_{1s} data for V_3Si [102] are plotted semilogarithmically in Fig. 2.13 as a function of T_c/T , where $T_c = 15.35\text{ K}$. Results are given for four different field values at temperatures in the SC state which extend down below $T_c/10$. At higher temperatures the data points asymptotically approach the dashed line which represents BCS behavior, i.e. $T_{1s} \propto \exp \Delta_0/k_B T$, where $\Delta_0 = 1.76 k_B T_c$. T_{1s} veers away from the BCS curve at $T_c/T \geq 4$, then ranges up to values more than three orders of magnitude longer than its value at T_c . The flattening of these curves is suggested to be caused by spin diffusion to the normal cores, which then becomes the only effective T_1 mechanism at the lowest temperatures. If the spin diffusion time, estimated below, is not an impediment, then at the lowest temperature we should have

$$\frac{T_{1n}}{T_{1s}} = \frac{h\xi_0^2 H}{\Phi_0}. \quad (2.3.19)$$

where h is a numerical factor of order unity. Equation (2.3.19) simply states that the normal T_1 should be diluted by the ratio of $h\xi_0^2$ to the area per fluxoid Φ_0/H . First, we note that $1/T_{1s}$ should be linear in H , as is clearly the case in Fig. 2.13. With the estimate $\xi_0 \simeq 25 \text{ \AA}$ for V_3Si given above, we find $h = 1.9$, so that the effective area of normal-state relaxation is a circle of radius slightly smaller than ξ_0 for each fluxoid. The corresponding spin diffusion times for the results in Fig. 2.13 we can estimate with

$$t_{diff} \sim \frac{d^2}{4D_{sp}}, \quad (2.3.20)$$

where d is the distance between fluxoids and D_{sp} is the spin diffusion constant. Taking $d = [2\Phi_0/\sqrt{3H}]^{1/2}$ and $D_{sp} \sim 10^{-12} \text{ cm}^2\text{s}$ [108], we find $t_{diff} \sim 13 \text{ s}$ at $H = 4450 \text{ G}$. This is an order of magnitude less than T_1 itself, lending credence to the use of (2.3.19).

While the foregoing scenario gives an appealingly straightforward interpretation of the V_3Si data for T_{1s} , there did arise in the literature a rather knotty problem in connection with this interpretation. Genack and Redfield suggested some time later [109] that the spin diffusion relaxation mechanism in type-II superconductors would not work, because it did not conserve energy. We give the essence of their argument here, then cite further work which provides something of an antidote to this objection.

If spin diffusion takes place along a field gradient, then the simple flip-flop events between neighboring nuclei no longer conserve energy. The difference in Zeeman (field) energies has to be taken up by the spin-spin (usually dipolar) interactions. Viewing this process thermodynamically, the dipolar reservoir then quickly becomes overheated and must, itself, relax to the lattice. The total relaxation process by spin diffusion is thus formulated as a dual process, with Zeeman (magnetization) and dipolar energies both diffusing to the normal cores in the mixed superconducting state. These processes were analyzed in [109] and found to be too slow to provide the observed T_1 processes in V metal [101]. It was concluded that these clearly observed diffusion-like T_1 processes must originate in some other way [109].

The problem is, of course, that no other ideas to explain type-II relaxation have been forthcoming. However, more recently, this problem has been revisited in terms of basically the same ideas, but using more sophisticated mathematical methods (see [110] and references cited therein). These authors have analyzed in detail the relaxation curves of ^{51}V in V metal at $T \ll T_c$ taken from [101] in terms of spatially varying Zeeman and dipolar spin temperatures. They find a good fit to the vanadium data, where the dipolar relaxation time constants are relatively short, thus not obstructing the longer diffusion-mediated Zeeman T_1 's.

It seems, then, that the phenomenology of (2.3.19) is basically correct, so that low-temperature, type II T_1 behavior is clearly understood. This is very important for the interpretation of T_1 data for high- T_c systems as well. However, as we shall see, the fundamental behavior of T_1 in high- T_c compounds involves SC gap symmetries which

usually have line nodes, giving power-law behavior at low temperatures [11]. Thus, the issues regarding T_1 data analysis differ somewhat from those of d-band SC metals discussed here. Nonetheless, the spin-diffusion-to-normal-cores T_1 mechanism in the mixed state has been found to play a significant role in the phenomenology of cuprate superconducting T_1 effects. The understanding of this effect gained with ordinary 3d metals will be an important resource in the chapters to follow.

The NMR Probe of High-T_c Materials and Correlated
Electron Systems

Walstedt, R.E.

2018, XIII, 323 p. 124 illus., 13 illus. in color., Hardcover

ISBN: 978-3-662-55580-4